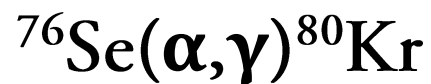


Measurement of the Cross
Section of the Astrophysically
Significant Reaction



DANIEL GOLTON

Master of Science by Research

UNIVERSITY OF YORK

Physics

DECEMBER 2018

Abstract

The p-nuclei are a group of 35 nuclides on the proton-rich side of the valley stability with $A > 56$, which cannot be produced through either s- or r- processes. Though their exact production method is a matter of debate, one scenario involves consecutive (γ, n) photodisintegrations from r/s seed nuclei. As a branching point in this process, ^{80}Kr is an isotope of interest and in particular, the magnitude of its related (γ, α) reaction rate has a significant impact on the abundance of the related p-nuclide, ^{78}Kr . Determination of the cross section of the reverse kinematic reaction, $^{76}\text{Se}(\alpha, \gamma)^{80}\text{Kr}$ (which is more practical to analyse), can be utilised to more accurately characterise this (γ, α) reaction rate. DRAGON was used to observe this forward reaction at an astrophysical energy. Upon investigation of the data set, no recoils could be identified from the background and steps were taken to calculate an upper-limit on the number of recoils present. From this value an upper-limit on the cross section was calculated, which was found to be significantly lower than the predictions of current theoretical models.

Contents

Abstract	2
List of Figures	5
List of Tables	7
Acknowledgments	8
Declaration of Authorship	9
1 Introduction	10
1.1 P-Nuclides.....	10
1.2 Motivation.....	11
1.3 Previous Work.....	12
1.4 Thesis Outline.....	14
2 Theory	15
2.1 Reaction Rates.....	15
2.2 Cross Sections.....	15
2.3 The Gamow Window.....	17
2.4 Reciprocity Theorem.....	19
3 Experimental Techniques	20
3.1 Equipment.....	20
3.1.1 Windowless Gas Target.....	20
3.1.2 BGO Array.....	23
3.1.3 Elastic Scattering Detectors.....	23
3.1.4 Charge State Booster.....	23
3.1.5 Electromagnetic Mass Separator.....	24
3.1.6 Multichannel Plate Detectors.....	25
3.1.7 DSSSD.....	25
3.2 Experimental Method.....	26
4 Analysis	27
4.1 Beam Normalisation.....	27
4.2 Particle ID.....	28
4.3 Charge State Distribution.....	35
4.4 Efficiencies.....	36
4.4.1 Separator Efficiency.....	36
4.4.2 Live Time Efficiency.....	37
4.4.3 MCP Transmission Efficiency.....	37

4.4.4 MCP Detections Efficiency and DSSSD Efficiency...	37
4.4.5 BGO Efficiency.....	39
4.4.6 Final Coincidences Efficiency.....	39
5 Results and Discussion	41
6 Conclusion	44
Bibliography	46

List of Figures

1.1	Illustration of how the valley of stability shields p-nuclei from the neutron capture processes and β^- decays.....	10
1.2	Illustration of the γ -process.....	11
1.3	γ -process pathway, highlighting ^{80}Kr as a branching point.....	12
1.4	Modelled cross sections for the $^{76}\text{Se}(\alpha,\gamma)^{80}\text{Kr}$ reaction.....	13
2.1	Illustration of how the energy of nuclear reactants and the associated level-scheme of the product nucleus contribute to nuclear resonances.....	16
2.2	Illustration of the Gamow window.....	18
3.1	Schematic of the ISAC-1 facility at TRIUMF.....	20
3.2	Diagram of the apertures in the DRAGON windowless gas target.....	21
3.3	Exploded illustration of the windowless gas target.....	22
3.4	Illustration of the BGO detector array.....	22
3.5	Illustration of DRAGON.....	24
3.6	Photograph of one of the DRAGON MCP detectors.....	25
4.1	DSSSD energy coincidence spectrum.....	28
4.2	DSSSD energy vs MCP TOF spectrum with DSSSD energy, BGO energy cuts.....	29
4.3	DSSSD energy spectrum with an MCP TOF cut between 35-43 ns.....	30
4.4	MCP-rf TOF spectrum.....	31
4.5	DSSSD energy spectrum of peak at 95 MeV.....	32
4.6	MCP TOF spectrum showing counts from 95 MeV DSSSD energy peak.....	32
4.7	DSSSD energy vs sepTOF spectrum.....	33
4.8	DSSSD hit pattern.....	34
4.9	DSSSD energy vs sepTOF spectrum for the bin (5, 24) from the DSSSD hit pattern.....	34
4.10	sepTOF spectrum for the region around 1530 ns showing distribution of background counts.....	35
4.11	Distribution of charge states fractions for ^{80}Kr recoils at 25+ charge.....	36

4.12	DSSSD energy vs MCP TOF spectrum for attenuated beam run, 4667.....	38
5.1	Plot of the calculated cross sections and modelled cross sections within an astrophysically important energy range.....	42

List of Tables

4.1	Table of efficiencies and their systematic uncertainties.....	39
4.2	Table of final counts and their statistical uncertainties.....	40
5.1	Table of final cross sections and their uncertainties.....	41

Acknowledgments

I would like to extend my gratitude to the members of the TRIUMF team and original experimentalists, without whom this thesis would not have been possible. In particular, I would like to thank Annika Lennarz for her expert advice in using the DRAGON analyser package for ROOT and her input on the analysis.


I would also like to thank both my supervisor, Alison Laird, and Christian Diget, for their resilience in support, and for their roles as constant educators. This would have been a letter of resignation, not a thesis, if not for them.

Finally, warm appreciation to my colleagues in the nuclear physics group: Joe Frost-Schenk, Ryan Llewellyn, Antonio Marquez and others, for their friendship during the more difficult periods of this journey, as well as valuable practical input on the project.

Declaration of Authorship

I, Daniel Golton, declare that this thesis titled, 'Measurement of the Cross Section of the Astrophysically Significant Reaction $^{76}\text{Se}(\alpha,\gamma)^{80}\text{Kr}$ ' and the work presented in it are my own. I confirm that:

- This work was done wholly or mainly while in candidature for a research degree at this University.
- Where any part of this thesis has previously been submitted for a degree or any other qualification at this University or any other institution, this has been clearly stated.
- Where I have consulted the published work of others, this is always clearly attributed.
- Where I have quoted from the work of others, the source is always given. With the exception of such quotations, this thesis is entirely my own work.
- I have acknowledged all main sources of help.
- Where the thesis is based on work done by myself jointly with others, I have made clear exactly what was done by others and what I have contributed myself.

Signed  _____

Daniel Golton

December 2018

Chapter 1

INTRODUCTION

Over their lifetimes, stars are responsible for creating nearly all the elements synthesised in the universe. Through fusion processes in their cores, and other processes occurring in their higher layers, such as the *s*- and *r*-processes, elements from helium up to some of the heaviest isotopes in existence are created and, eventually, dispersed at the death of the star. With these stellar objects being the source of much of the raw material that makes up everything around us (including our own bodies), it is no wonder that one of the key pursuits in modern physics is trying to understand how these elements are formed by stars and in what abundances. This field of study is known as nucleosynthesis and marries the disciplines of nuclear physics and astrophysics together. Studying nucleosynthesis requires both the experimental and theoretical approaches to science, using data from experiments to refine the models used to describe and predict physical phenomena.

1.1 P-NUCLIDES

There are 35 nuclides on the proton-rich side of the valley of stability that cannot be synthesised through neutron-capture or beta-minus processes, such as the *s*- and *r*-processes (see figure 1.1). These naturally occurring nuclei are known collectively as the *p*-nuclei, and their production is a matter of ongoing investigation. Both the location and the full mechanism by which these nuclides are produced are not fully understood.

The model currently favoured (though others have been proposed [1]) involves the nuclei being produced in the ONe shell of certain massive stars during the process of core collapse [1], but this fails to account for the observed solar abundances of the nuclei in question. Moreover, the



Figure 1.1: The *p*-isotopes are shielded from *r*-process decay chains by the *s*-process and stable isotopes. Taken from [1].

ambiguously named p-process, which refers to the exact production mechanisms of the p-nuclei is relatively unexplored at an experimental level and data are scarce [1].

One such mechanism is the (p, γ) reaction. A sequence of these reactions from low mass nuclides can carry an isotope into the region of the valley of stability where the p-nuclei can be found. The

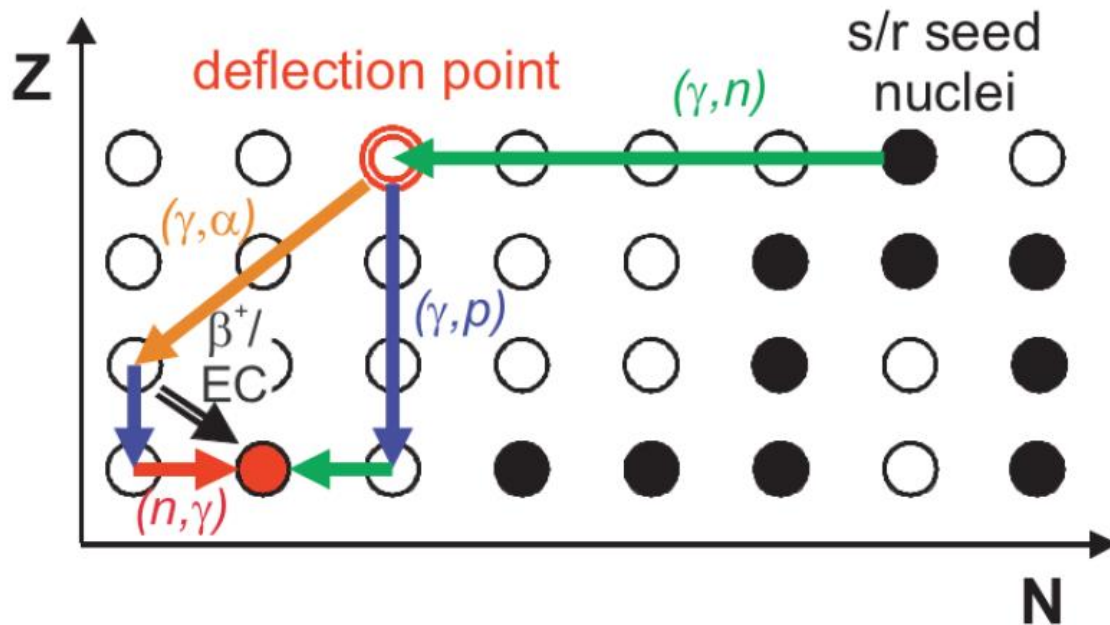


Figure 1.2: The gamma-process consists of (γ, n) photodisintegration that are occasionally diverted at deflection points by either (γ, α) or (γ, p) reactions. Taken from [1].

contribution of this particular phenomena is limited though, by the realities of the astrophysical energies that these nuclei would be produced at. Coulomb repulsion, the very high temperatures needed and the dominance of (γ, p) photodisintegrations are all contributing factors to this.

Fig 1.2 shows one of a collection of independent processes contributing to the production of p-nuclides. Another of these is known as the gamma-process [1]. This involves a series of (γ, n) disintegrations from a seed nucleus in the s/r chains that move towards the p-nuclides (see figure 1.2), until they are overtaken by (γ, α) and/or (γ, p) reactions.

1.2 MOTIVATION

The gamma process provides a method by which the p-nuclides can be produced at astrophysical energies. Through neutron-photodisintegrations an isotope can move towards the proton-rich side of the valley of stability. Eventually however, the (γ, p) or (γ, α) reactions will become dominant and the path shifts to a lower Z-nuclide. The isotopic location at which these events occur are known as "branching points" [2]. At branching points, there exists competition between different reaction channels, and changes to the environment, such as a change in isotopic energy or temperature can impact the dominance of certain reactions and consequently the prominence of certain isotopes. When determining the abundance of a given p-nuclide, knowing the location of the relevant deflection points is vital.

Only a few reactions in the gamma-process have a noticeable impact on abundances. One of these reactions is $^{80}\text{Kr}(\gamma,\alpha)^{76}\text{Se}$, because ^{80}Kr is a branching point. If this reaction or the (γ,p) process dominate over (γ,n) at ^{80}Kr then the subsequent production of the p-nucleus ^{78}Kr would be limited (see figure 1.3).

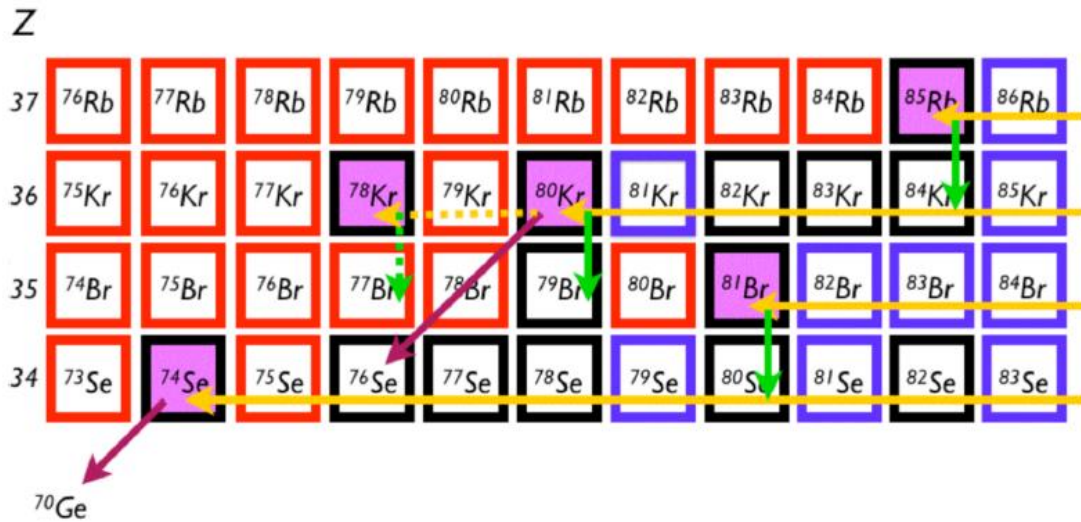


Figure 1.3: Possible gamma-process pathway, showing ^{80}Kr as a branching point for the process [2]. If the (γ,α) or (γ,p) reactions start to dominate over the (γ,n) photodisintegrations at this point, the pathway will be diverted to either the Br or Se chains. Taken from [3] (can also be seen in [4]).

Calculating the reaction rates for the gamma-process is difficult though, because high-mass nuclei have great level densities and high Coulomb barriers. Capture reactions therefore need high temperatures to overcome the energy requirements. This means the reactions typically occur in a variety of excited states. Lab experiments can only give data on the cross section of a reaction with the target nuclei in the ground state though, so any conclusions drawn experimentally must be supplemented by theory. Nonetheless, without such data (and there is very little in this energy-region of interest) it is difficult to constrain or refine these theoretical predictions [1]. So, data must be acquired.

There is a direct relationship between a reaction rate at a given energy and the cross section at the same energy. By calculating the cross section of a reaction at the relevant energy, the reaction rate of that reaction can be inferred. The aim of this project was to determine the cross section of the $^{80}\text{Kr}(\gamma,\alpha)^{76}\text{Se}$ reaction. This value cannot be found directly via experimentation, both because of the energies required to produce meaningful data and the difficulty of producing a stable gamma beam; the cross section of the reaction can be inferred however, from the cross section of the time reversed reaction: $^{76}\text{Se}(\alpha,\gamma)^{80}\text{Kr}$.

1.3 PREVIOUS WORK

As previously mentioned, data for this energy region is scarce, however this thesis (the present

work) is not the first to explore the $^{76}\text{Se}(\gamma,\alpha)^{80}\text{Kr}$ reaction. This same reaction has been observed to determine the cross section at beam energies of 1.51 MeV/u and 1.43 MeV/u [4]. The experimental method utilised was quite similar to the one described in this thesis, with an accelerated beam of charged ^{76}Se ions directed at DRAGON's windowless gas target, containing pressurised He gas. The recoils were then bent through the mass-separator to filter out leaky beam, before being detected by the MCP detectors. The difference between the experiment described in [4] and the one described here is that the author of [4] made use of DRAGON's ion-chamber (IC) instead of the DSSSD for the purposes of particle identification. The IC contains an isobutane gas and has four anodes for collecting charge.

Fast ions, like recoil products, ionise this gas as they travel through the chambers. Pairs of ions and free electrons are produced and the positively charged ions are attracted to the anodes positioned along the length of the chamber, inducing a current in them. This represents an output signal from the detector. By placing these anodes at different positions along the length of the chamber, the energy loss of the incident ions can be charted as a function of depth. As different nuclei loose energy at different rates in the gas, with more massive, or more charged isotopes losing energy more quickly, this data can then be used in the process of particle identification (particle ID) to discover the yield of recoils in the experiment and generate a value for the cross section.

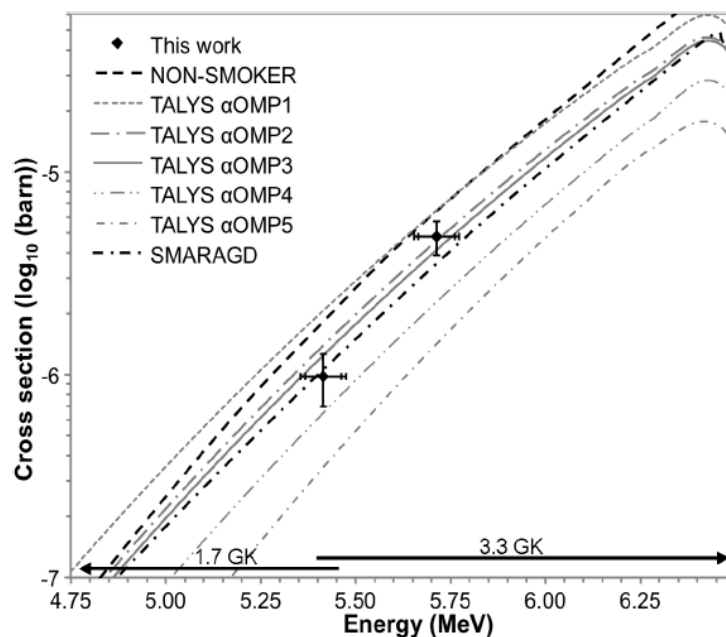


Figure 1.4: The cross sections for the $^{76}\text{Se}(\alpha,\gamma)^{80}\text{Kr}$ reaction between the centre-of-mass energies of 4.75-->6.5 MeV as modelled using a variety of computational models by [5]. TALYS is a modelling software for simulating nuclear reactions. The five curves produced using TALYS used different α optical modelling potentials (α OMP). The NON-SMOKER code used to produce the long-dashed curve uses the same α OMP as TALYS α OMP2, as well as the same nuclear-level density model, but with different starting parameters. SMARAGD is an improved version of NON-SMOKER that supersedes NON-SMOKER results [6]. The two data-points with error bars are the calculated cross sections for the $^{76}\text{Se}(\alpha,\gamma)^{80}\text{Kr}$ reaction at the centre-of-mass energies 5.42 MeV and 5.72 MeV, calculated by [4, 5]. The figure itself is taken from [5].

In the motivation it was mentioned that experimental data is limited in its effectiveness when in isolation from theoretical predictions, especially in the field of nuclear astrophysics. For [4] to measure the success of the experiment and subsequent analysis, the author compared his results to predictions made by the NON-SMOKER model. NON-SMOKER is a code that allows calculations of cross sections based on the Hauser-Feshbach (HF) model of nuclear reactions. The Hauser-Feshbach model makes assumptions about nuclei and their possible energy levels to allow for the calculation of nuclear cross sections. NON-SMOKER uses a variation of HF [6] to predict the cross sections of a given reaction at a range of energies. The NON-SMOKER cross sections for the centre-of-mass energies $4.75 \rightarrow 6.5$ MeV, for the $^{76}\text{Se}(\alpha, \gamma)^{80}\text{Kr}$ reaction, can be seen in figure 1.4.

Similarly, to how [4] contrasted its results with the predictions of this model, so shall this thesis do so in the results section, although the results will here be compared to NON-SMOKER's successor model, SMARAGD, as results from SMARAGD supersede those produced by NON-SMOKER [6]. This will provide context to the results of the experiment and in doing so highlight potential areas for further investigation pertaining to this particular reaction cross section.

1.4 THESIS OUTLINE

This thesis will focus on a similar experiment to [4], that aims to contribute to the understanding of nucleosynthesis. The experiment, performed at TRIUMF Nuclear Laboratory in Vancouver, examines the $^{76}\text{Se}(\alpha, \gamma)^{80}\text{Kr}$ reaction. Understanding this reaction is crucial to understanding its time-reversed counterpart-reaction, $^{80}\text{Kr}(\gamma, \alpha)^{76}\text{Se}$, which represents a key branching point in a chain of reactions that can lead to the production of p-nuclei, a special group of nuclei heavier than ^{58}Fe , the production mechanisms of which are not well understood.

This chapter of the thesis has given some background information to the above experiment and explained in more detail its aims and motivation. Chapter 2 presents the theory behind the experiment and clarifies some key terms that will be later used in the analysis. In Chapter 3 there will be an overview of the facilities and equipment used in the experiment. Chapter 4 presents the analysis of the data gathered and features figures demonstrating the reasoning behind decisions made during said analysis. Chapter 5 displays the results of the experiment and Chapter 6 presents a summary of the conclusions drawn.

Chapter 2

THEORY

In general, the end goal of nuclear-astrophysical experiments is to better characterize the reaction rate of the reaction being investigated, in a stellar environment. The problem with studying astrophysical reactions in the laboratory is that these reactions typically involve large Coulomb barriers, whilst simultaneously occurring at temperatures that allow for only sub-Coulomb barrier energies. To counter this, laboratory experiments make use of thick stationary targets, with high densities of target nuclei, and advanced particle ID systems placed with maximum possible coverage around the target to ensure the few successful reactions are captured by the detection system. Having a thick target also allows for a range of reaction energies to be observed as the beam loses energy travelling through the target.

2.1 REACTION RATES

In a nuclear environment, it is the reaction rates of the various reactions possible, given the starting isotopes, that determine the dominance of certain reactions over others and consequently the final abundance of certain isotopes over others. In modelling stellar explosions and the consequent production of the p-nuclides then, it is important to accurately characterise the reaction rates of reactions possible in the stellar environment being simulated.

What causes certain reactions to dominate an environment is having a high reaction rate, which allows for the rapid utilisation of the isotopes involved as reactants of a given reaction. Reaction rate being high is dependent on a number of factors that all contribute to how likely a reaction is to happen in a particular environment, including the availability of energy (often characterised by the temperature of the environment), and the availability of the constituent reactants (isotopes and particles such as protons, neutrons, alphas, beta and gammas). This probability of a reaction occurring is known as the “cross section” of the reaction and is related to the reaction rate of a reaction by the equation:

$$r_{01} = N_0 N_1 \langle \sigma v \rangle_{01}, \quad (1)$$

where r_{01} is the reaction rate of two unique particles, 0 and 1, $N_0 N_1$ is the total number density of pairs of 0 and 1, and $\langle \sigma v \rangle_{01}$ is the average reaction rate per particle pair, consisting of v , the relative velocity of the pair (in this case representing the distribution of velocities present in a stellar environment), and σ , the cross section of the reaction.

In order to accurately characterise the reaction rate, the cross section of the reaction under the same conditions (energy region specifically) must first be characterised.

2.2 CROSS SECTIONS

The cross section describes the reaction rate as a function of energy.

$$\frac{N_R}{t} = \frac{N_b N_t}{t A} \sigma, \quad (2)$$

where $\frac{N_R}{t}$ is the yield per second, $\frac{N_b}{t}$ is the beam current, $\frac{N_t}{A}$ is the target density and σ is the cross section, which is proportional to the probability that the reaction occurs, expressed in units of area, normally barn³.

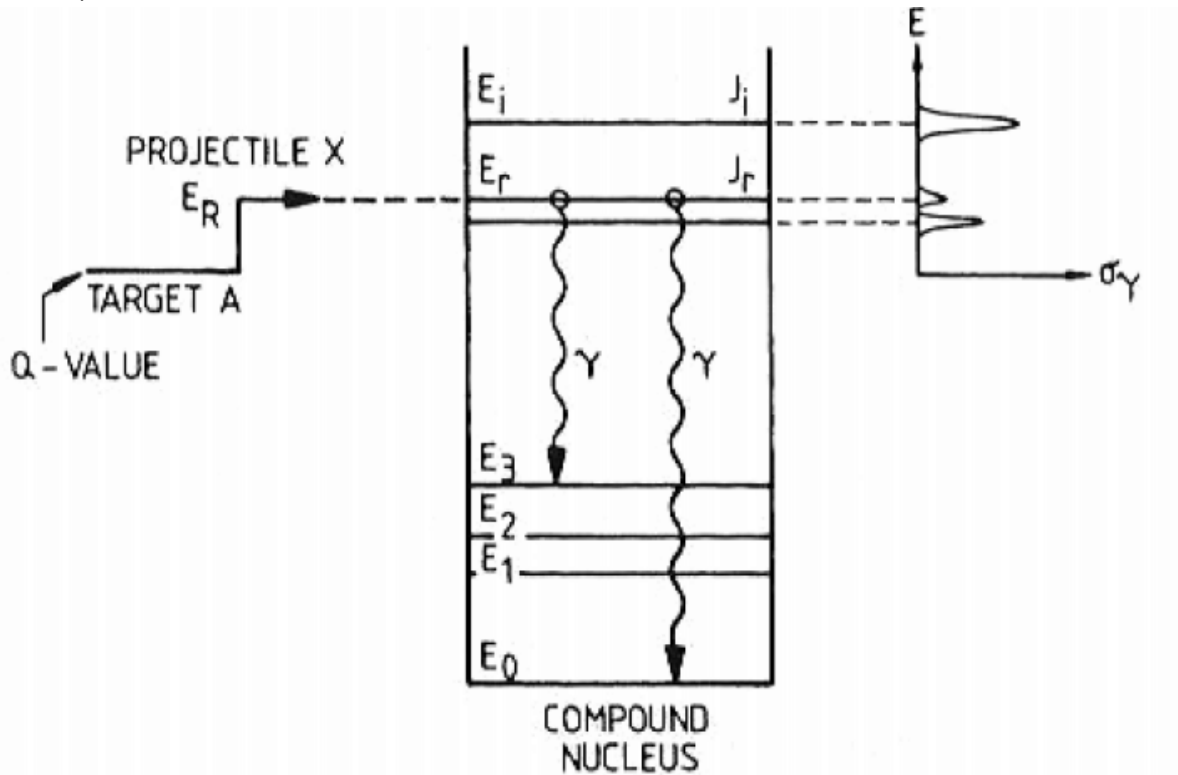


Figure 2.1: Diagram showing how the energy going into a reaction is connected to the level scheme of the compound nucleus it would produce. Reactions are far more likely when they match the energy of an excited state in the product nucleus. This is known as a resonance. Taken from [7].

Sometimes a fusion reaction passes through an intermediate excited state before decaying to a final state e.g. in the $^{18}\text{F}(p,\alpha)^{15}\text{O}$ reaction, ^{18}F takes on another proton, becoming an excited state of ^{19}Ne , before emitting an alpha-particle to become ^{15}O . Transitions like this increase a reaction's cross section because of an overlap between the reaction channel and the excited states of the transition nuclei. When a nucleus is subject to interactions with particles of a certain species, the probability of a specific reaction is limited unless the energy of the interacting particles is in the region of a transition energy. The requirement is that the sum of the ground state energy of the initial nucleus and the added kinetic energy in the reaction is equivalent to an excited state of the compound nucleus (see figure 2.1). Such transitions are known as resonances and greatly impact the abundances of certain isotopes.

The cross section is not delta-value centred on one of these resonances but a function that drops off around either side of a resonance. The function describing this curve is the Breit-Wigner function:

$$\sigma(E) = \left(\frac{\lambda^2}{4\pi}\right) \left(\frac{(2J+1)(1+\delta_{ab})}{(2j_a+1)(2j_b+1)}\right) \left(\frac{\Gamma_a\Gamma_b}{(E_r-E)^2 + \left(\frac{\Gamma}{2}\right)^2}\right), \quad (3)$$

where J is the spin of the compound system, δ_{ab} is the Dirac-delta function which is equal to 1 when $a=b$ and equal to 0 at all other times, $j_{a,b}$ are the spins of the reactant particles, λ is the de Broglie wavelength and $\Gamma_{a,b}$ are the partial widths of the entrance and exit channels.

In a lab setting, calculating the cross section as above is not practical as isolating a single energy within a thick target is impossible. Instead, the ratio of reactions to beam particles is calculated. This is known as the yield per incident ion:

$$Y = \frac{N_R^{det}}{N_b\eta_{coinc}}, \quad (4)$$

where η_{coinc} is the combined efficiency of the equipment used to detect counts and gather the data.

In a target where energy loss per unit length is constant, this can be rewritten as:

$$Y = \sigma \frac{N_t}{A} = \sigma \frac{N_t}{V} \Delta x, \quad (5)$$

where Δx is the target thickness and $\frac{N_t}{V}$ is the target's particle density in volume.

This thesis will seek to extract a yield from the experimental data, which combined with known values for target thickness and target particle density, can be used to calculate the cross section of the reaction, σ :

$$\sigma = Y \frac{V}{N_t} \Delta x. \quad (6)$$

2.3 THE GAMOW WINDOW

The cross section of a reaction is of course, dependent on the energy available to the particles involved. This experiment and others involving the same reaction have chosen specific energies for the beam, and therefore expect different values for cross section. Determining which energies should be explored involves knowing at what energies it is possible for the reaction to occur, theoretically speaking.

The barrier preventing nuclei and other particles from interacting directly is the Coulomb Barrier, which for positively charged nuclei keeps them from fusing. The energy required to overcome this barrier is given by:

$$E_{Coulomb} \cong \frac{Z_0 Z_1 e^2}{r_0},$$

where Z is the proton number of the nuclei involved, e is the charge of a single proton, and r_0 is the radius at which nuclear attraction overcomes coulombic repulsion. For two protons this value is around 1 MeV.

The kinetic theory of gas stipulates that gas particles have kinetic energy due to their motion and collisions with one another. Temperature is a way of characterising the kinetic energy of particles in a medium. Maxwell-Boltzmann determined that temperature is proportional to the mean kinetic energy of a medium:

$$E = \frac{1}{2}mv^2 = \frac{3}{2}kT, \quad (8)$$

where k is the Maxwell-Boltzmann constant, 1.38×10^{-23} J/K.

Using this equation, it can be seen that even though the temperatures found in a stellar environment are extremely high, they are still not enough to overcome the Coulomb Barrier. Considering the core of the sun, where fusion of individual protons occurs, the temperature is $T_C \approx 1.5 \times 10^7$ K. Using the Maxwell-Boltzmann constant, this only gives an energy of $E \approx 1$ keV, a factor of 10^3 from the energy needed to overcome the coulombic barrier.

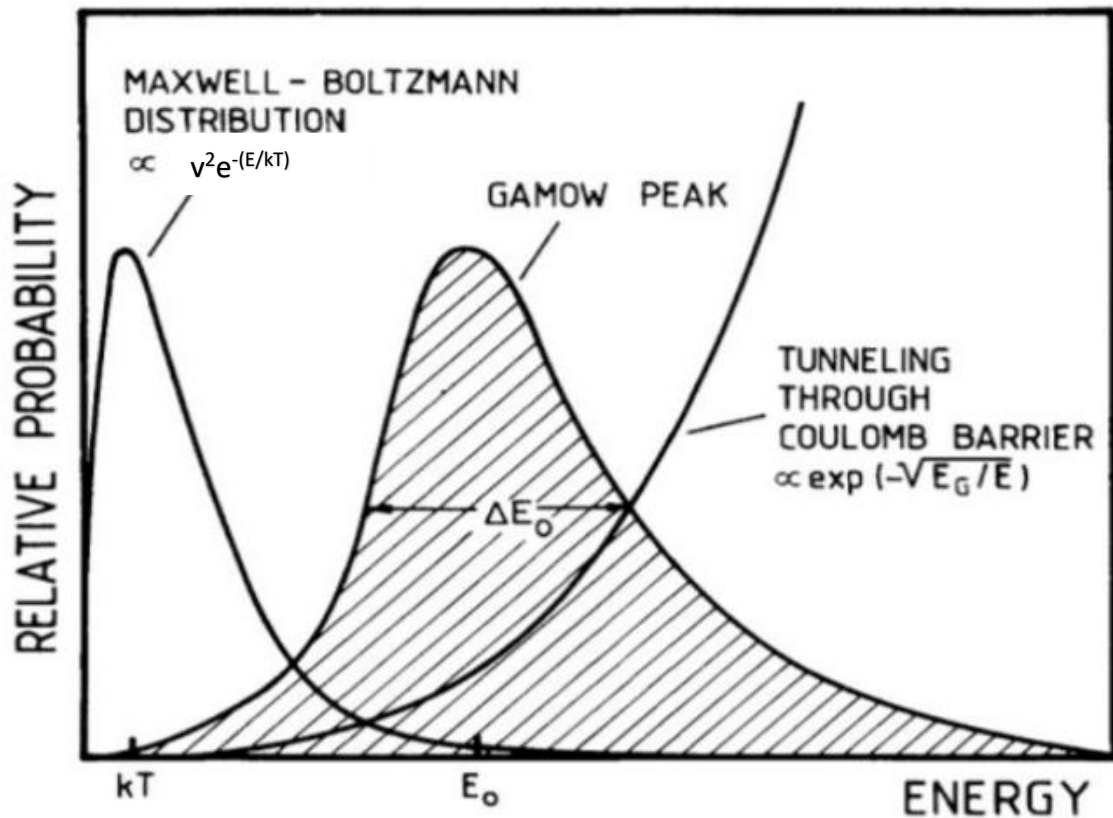


Figure 2.2: The Gamow window and its relationship to the Maxwell-Boltzmann distribution and the probability of tunnelling through the Coulomb Barrier. Taken and edited from [8].

It is nonetheless possible for fusion to occur. Though it only occurs with low probabilities, it is possible for particles that do not have enough energy to overcome the Coulomb Barrier to engage in quantum tunnelling and interact with a target nucleus anyway. This becomes more likely as the kinetic energy of the particle in question increases. The Maxwell-Boltzmann distribution, the distribution of kinetic energies among particles in a medium of a given temperature, also means that some particles in a medium, of seemingly too low a temperature to allow for interaction between nuclei, will have a high enough energy to achieve quantum tunnelling.

As can be seen in figure 2.2, the cross-over between these two regions, the tail of the Maxwell-Boltzmann distribution and the beginning of the region describing the probability of a particle having sufficient energy to penetrate a nucleus, is known as the Gamow window, and is the energy region in which the cross section is sufficiently large for a reaction to occur. This window is roughly Gaussian in shape and encompasses a relatively small energy range for non-resonant reactions.

It is from this window that the beam energy for this and other similar experiments was selected.

2.4 RECIPROCITY THEOREM

It was established in section 1 that the experiment is not directly investigating the cross section of interest. Sometimes it is not possible to observe a given reaction due to experimental constraints, in this case the difficulty of producing a stable photon beam and getting a high enough beam energy to match the energy available in a high-temperature astrophysical environment. In these cases, it is possible to instead observe the reverse reaction and then calculate the cross section of the forward reaction from the result. The relationship between these two values is as follows:

$$\sigma_{Bb \rightarrow Aa} = \frac{\sigma_{Aa \rightarrow Bb} (2j_A + 1)(2j_a + 1) k_{Aa}^2 (1 + \delta_{Bb})}{(2j_B + 1)(2j_b + 1) k_{Bb}^2 (1 + \delta_{Bb})}, \quad (9)$$

for the reaction $A(a,b)B$ where A is the initial nucleus (the target particle in this instance), a is the initial reactant particle (the beam particle in this instance), and B and b the products of the reaction. In this $B(b,a)A$ being the forward reaction to $A(a,b)B$'s reverse reaction. δ_{Bb} is a Dirac-delta and k is the wave-number of a free particle [9].

Chapter 3

EXPERIMENTAL TECHNIQUES

The TRI University Meson Facility (TRIUMF) is Canada's national particle and nuclear physics research laboratory and is located on the University of British Columbia campus in Vancouver. The experiment that is the focus of this thesis was performed there, and this next section will describe both the facility and the equipment used to conduct the experiment.

The ISAC (Isotope Separator and Accelerator) facility at TRIUMF uses accelerated radioactive beams to measure cross sections, and features a cyclotron, isotope source and DRAGON (Detector of Radiation And Gammas of Nuclear reactions). For this experiment isotopes for the beam were drawn from OLIS, an Offline Ion Source, and then accelerated down the line to the experimental hall, ISAC-1 (see fig 3.1).

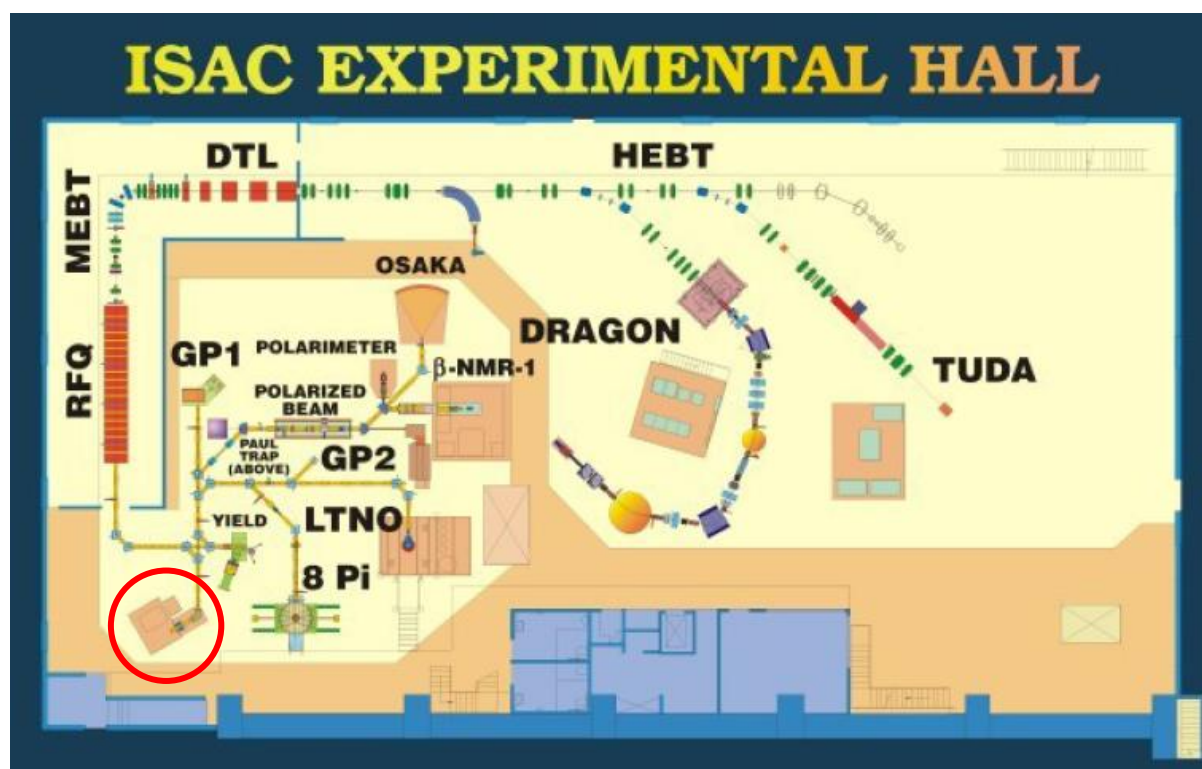


Figure 3.1: Schematic of the ISAC-1 facility at TRIUMF. It shows the path that the beam particles in the $^{80}\text{Kr}(\gamma, \alpha)^{76}\text{Se}$ experiment take from OLIS (circled by the author) to DRAGON itself. Taken from [4].

3.1 EQUIPMENT

3.1.1 Windowless Gas Target

Electromagnets accelerate isotope beam towards the windowless gas target. Before this is reached however, it is possible to take a current reading with one of the system's four Faraday cups.

The target does not suspend the gas in glass, plastic or some other material but uses pumps to keep

the gas in the beam's path and feed leaking gas back into the target [see figure 3.2]. The pressure regulation in the target ensures that the gas density is uniform over the 11cm-long target cell between the two beam apertures inside the target. Ultimately, the length of 11cm was chosen, because making the target too thick would increase the apparent beam spot size, limiting the efficacy of the electromagnetic mass separator (EMS). Not thick enough though, and the yield would be too low. The actual distance between the two beamline apertures (the span of which is a little greater than the length of the target cell itself) can vary between 12→13cm [10] depending on target gas pressure.

The target chamber was designed for a pressure of 4.5 Torr, but this experiment required pressures of 8 Torr and above as lower pressures would not have produced sufficient yield for meaningful results. Accepting higher pressures than this would have required more expensive pumps to recirculate gas post-target.

After the main chamber, the gas is differentially pumped (see fig 3.2), thereby reducing the pressure to 10^{-6} by the beginning of the EMS. This guarantees minimum contamination in the particles exiting the target. A higher density of gas downstream of the target could cause charge changing reactions that would weaken the suppression factor of the EMS.

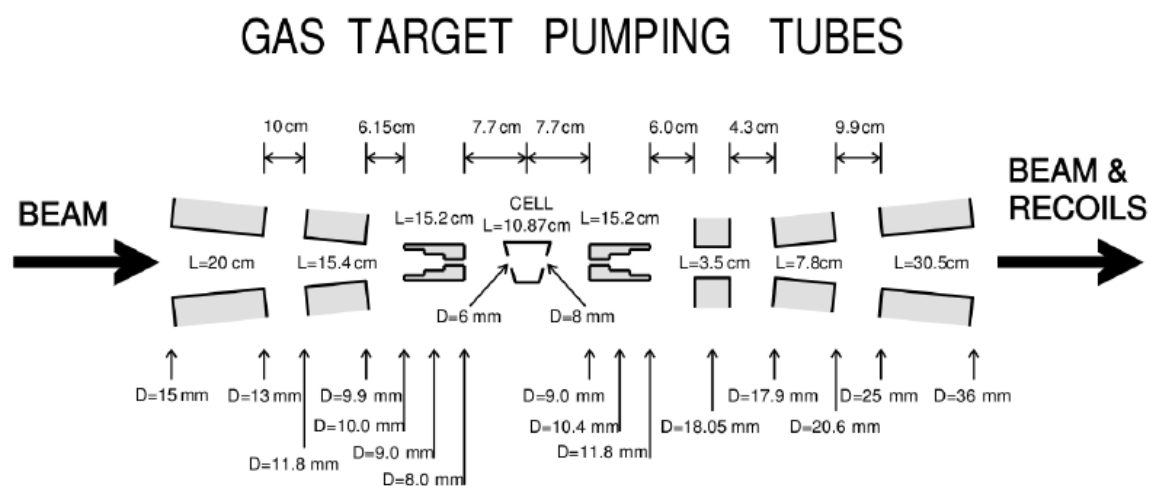


Figure 3.2: The apertures of the DRAGON windowless gas target. Taken from [10].

The design of the target cell (see fig 3.3) itself is a compromise. To count the gamma rays efficiently, a smaller chamber is needed to allow for a compact array of BGO detectors surrounding it (see fig 3.4). This however, must be balanced with a need for good pumping regions adjacent to the chamber. A number of parts of the pumping equipment run into the bottom of the target chamber. The chamber itself is made of aluminium, to limit the surplus of absorbable mass between the source and the BGO detectors. This design of the target chamber and the arrangement

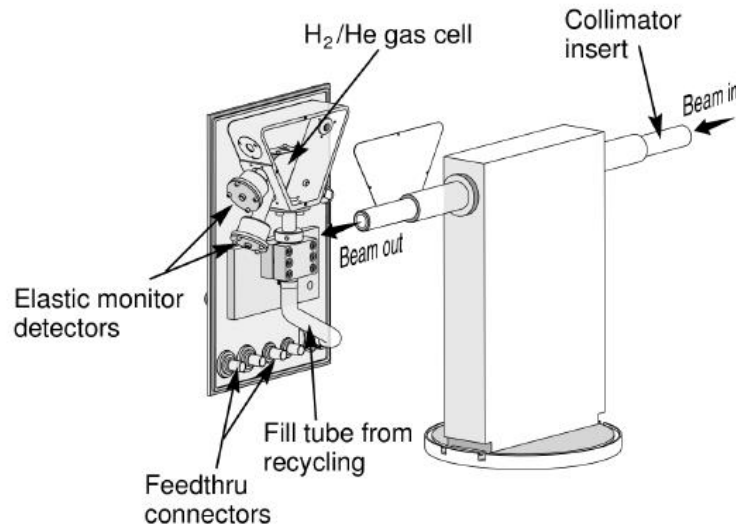


Figure 3.3: Illustration of the DRAGON windowless gas target, with the side piece and inner workings exploded. Taken from [10].

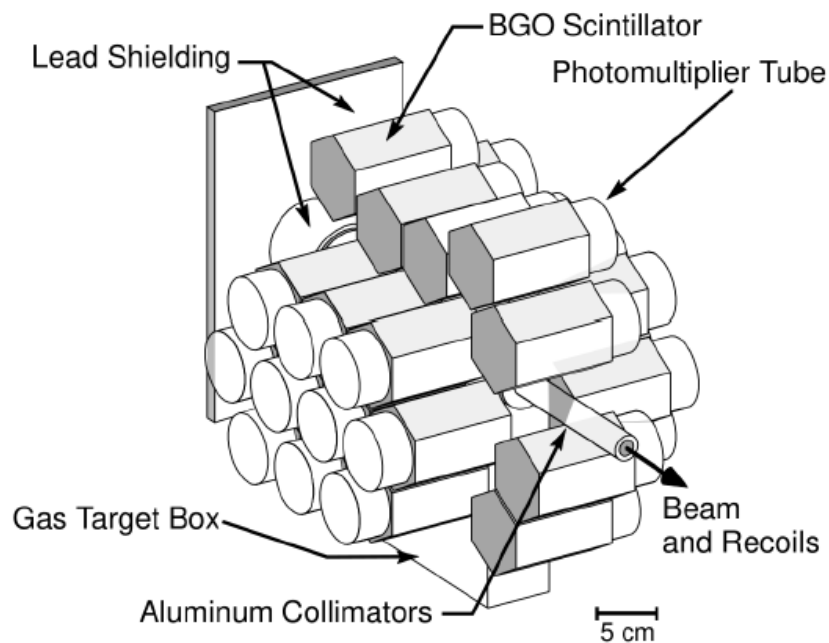


Figure 3.4: The arrangement of BGO detectors in the array that surrounds the windowless gas target. The BGO crystals are positioned so as to provide maximum coverage for gammas radiating from the target. Taken from [10].

of the BGO array allows for approximately 80% of the (4π) solid angle to be covered by the array [10].

When the beam collides with the gas, two things typically occur. Either the target particle is absorbed by the beam particle and a resultant gamma is ejected, in which case the gamma may be detected by the BGO (Bismuth-Germinate) array that surrounds the target on either side, or the two particles are elastically scattered from one another. In the latter case, it is possible that the

scattered target particle is detected by one of two surface-barrier (sb) detectors.

3.1.2 BGO Array

An array of 30 BGO scintillation detectors surrounds the target. These hexagonal columns are arranged (see fig 3.4) in a formation that allows for 79%→82% solid angle coverage, with two banks of 10 tessellated detectors and 10 more placed along the thin edges of the target.

The BGO array measures the energy of prompt gamma rays emitted from the target. This starts a clock that registers when its partner particle (the coincidence) reaches the DSSSD (double-sided silicon strip-detector) at the far end of DRAGON's EMS, just beyond a pair of MCPs (multi-channel silicon strip detectors). This allows the experimenter to discriminate between "single" counts and those with associated gamma-ray coincidences when analysing data from DRAGON.

Monte Carlo simulations involve simulating a scenario (in this case the emission of gamma rays from the target with the proposed orientation of the BGO array) many times to quantify the relationships between the different parts of a setup. These were used to help optimise the efficiency of this array for detecting 1-10 MeV gammas originating from the gas target [10]. The array was designed with two major considerations in mind: (1) to count fast so as to be able to pick out and reject 511 keV gammas produced by spontaneous particle-antiparticle pair annihilation [11], and (2) to have an excellent energy resolution, in order to discriminate between captured gammas and the low-energy gammas, that can occasionally pile-up (appearing as if they were one higher-energy ray).

BGO crystals were selected as scintillators over other crystals for their simple exponential time-constant emission decay [12] and their high density [13], the latter of these making for an efficient, economical array. Each detector contains one such BGO crystal, surrounded by a mm-thick layer of MgO, which is highly reflective, to maximise detection efficiency. The two detectors upstream of the target are offset by 7.3cm to allow for lead shielding, designed to minimise the effect of 511 keV beam induced background from the target openings.

3.1.3 Elastic Scattering Detectors

As can be seen in figure 3.3, two ORTEC Ultra Cam Silicon detectors are mounted within the central chamber of the target, one at a 30° angle to the beam and the other at 57°. These elastic-scattering or surface-barrier (sb) detectors give particle counts that can be used to monitor the number of beam particles that passed through the gas-target during a run; the process of calculating this value is known as normalisation (see section 4.1).

3.1.4 Charge State Booster

Upon exiting the target, the heavy recoils do not have enough charge to be properly manipulated by the separator portion of the detector, which was built originally for particles of mass $A \leq 30$ [14]. So, all particles that successfully exited the target, beam and recoil, pass through a metal foil known as a charge-state booster (CSB), designed to boost the charge state of ions passing through it, by stripping them of their electrons [15].

In a higher charge state, the electrostatic dipoles that control which ions successfully navigate the electromagnetic mass separator (EMS) have more control over which ions make it through and allows for more choice when selecting which part of a recoil's charge state distribution to use.

The foil was designed using 350nm thick, aluminium windows [5], as carbon foils proved unable to withstand the 8.5 Torr pressures emanating from the gas target [15].

In this experiment, the charge of the ^{80}Kr recoils exiting the target was boosted up to 25+, to account for the high mass of the ion. There was of course a range of charge states produced, but this was the one chosen to provide an adequate balance between selection and yield.

3.1.5 Electromagnetic Mass Separator

After passing through the CSB, the remaining particles enter the electromagnetic mass separator (EMS). The separator has an acceptance cone of ± 20 milliradians and due to the way momentum is exchanged in the gas target, and the high masses of the particles involved, nearly all of the particles that exit the target are able to enter the separator. Here, a series of electrostatic and electromagnetic dipoles deflect particles in the beam round the curve of the EMS, with a field that is finely tuned to allow only particles of a certain mass and charge to stay on the path necessary to navigate the bend.

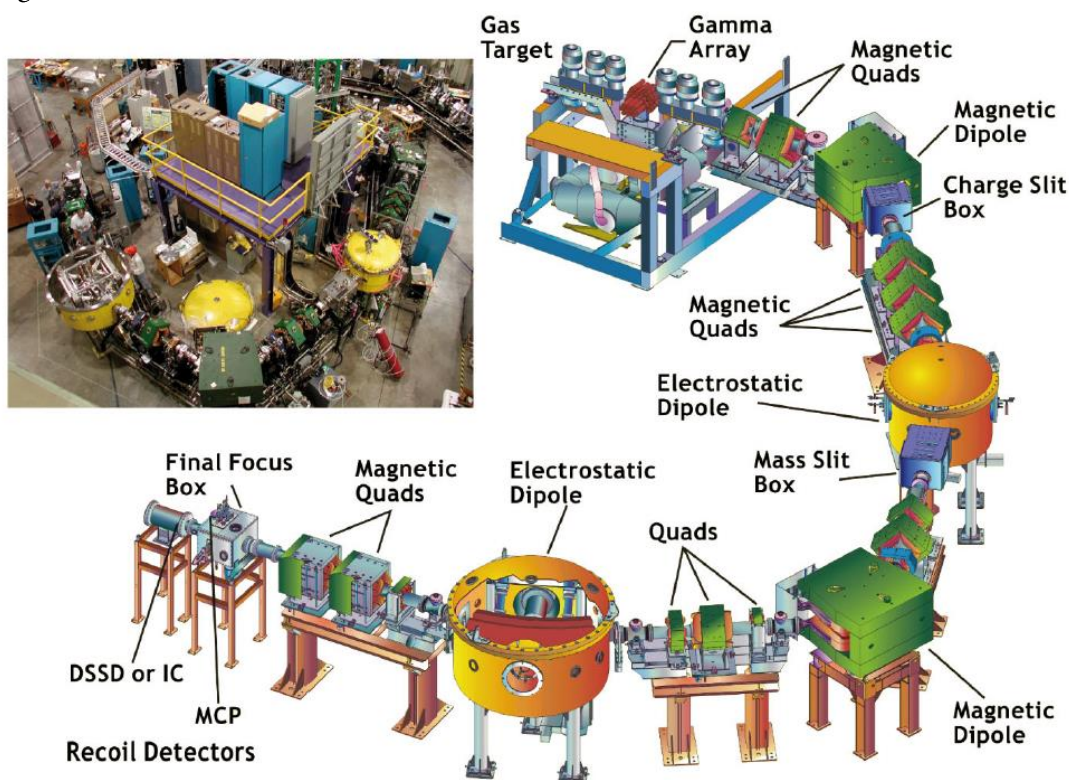


Figure 3.5: A schematic of DRAGON, displaying the various components of the EMS and their arrangement. Taken from [16].

The separator consists of a series of magnetic dipoles (M), magnetic quadrupoles (Q) magnetic sextupoles (S) and electrostatic dipoles (E). Arranged in the order (QQMSQQSE)(QQSMQSEQQ), they form two stages of mass separation (see figure 3.5). The dipoles of both species are used to separate the unreacted beam that accompanies the genuine recoil counts, whereas the quadrupoles and sextupoles are used for focusing the stream of ions. Each component is fitted with a Nuclear Magnetic Resonance probe, which can be used for measuring magnetic field strength at a high precision.

Typically, the number of leaky beam ions is far higher than the number of recoils produced in such an experiment, to the order of $\sim 10^{10} \rightarrow 10^{15}$ for astrophysical reactions [4]. The EMS must then be highly efficient at separating this beam from the recoils, so as to make any analysis that follows effective. Test measurements of the EMS have shown that it is capable of excellent beam suppression, reducing leaky beam to $\sim 10^{-10} \rightarrow 10^{-15}$ leaky beam events per beam ion on target [17]. It can also deliver recoils at the selected charge state to the end of the separator with an efficiency of $>95\%$ [4].

3.1.6 Multichannel Plate Detectors

After the EMS, the beam reaches a pair of Multichannel Plate detectors (MCPs). The DRAGON MCPs have a carbon foil positioned so that incident ions can release cascades of electrons as the beam passes through each detector. The electrons are then deflected away from the beam path by a grid of biased wires (also known as an “Electrostatic Mirror”), angled at 45° to the beamline [16]. Deflected electrons then meet the MCP itself and upon contact generate a fast timing signal (see figure 3.6 for this arrangement).

By having a pair of these MCPs, it is possible to calculate an accurate local time-of-flight over a section of the beamline. This value can be used to estimate the mass of ions in the beam, as particles of different masses and energies will have different velocities, and so can be used in the particle ID process of analysis. The carbon foil used in the MCPs is so thin that there is very little interference with the trajectories of the incident particles [4].

3.1.7 DSSSD

The final part of DRAGON is the DSSSD (Double-Sided Silicon Strip Detector). This detector, consisting of two layers of sixteen silicon detector strips, is designed to take an energy reading of

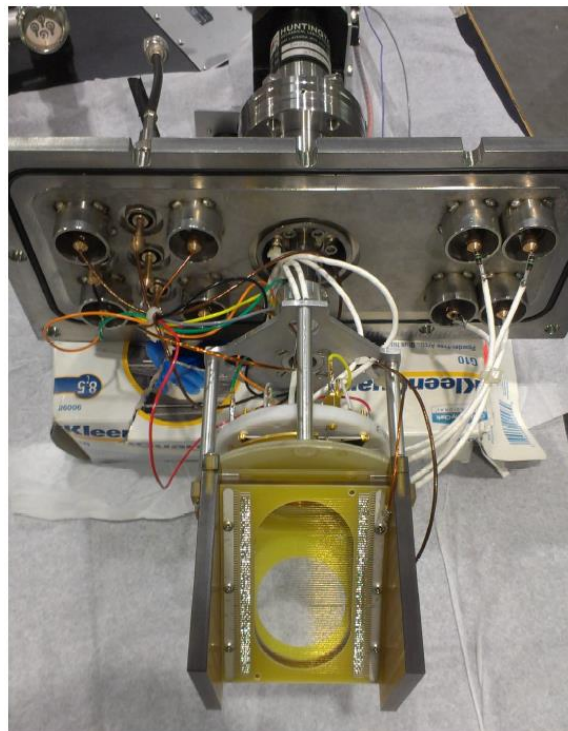


Figure 3.6: A photograph of one of the DRAGON MCP's with the carbon foil removed. The electrostatic mirror used to deflect the electrons can be seen just below the MCP itself, which is in the white plastic. Taken from [4].

ions that reach the end of DRAGON. The two layers of strips are arranged at right angles, the front strips measuring the horizontal position of the arriving particles, the back strips the vertical position. Between the two sets of strips, both the energy and pixel-position of an ion can be measured. The position of incoming particles is important because groupings of hits may suggest particles of a similar mass-energy ratio.

Sometimes ions hit the small gaps between strips in what are known as “inter-strip events”. In these events, the energy reading is distributed between the strips on both sides, leading to counts consisting of only part of an ion’s total energy. When looking at the energy spectrum of the DSSSD from a run, these events might be recognised by a small peak at approximately half the energy of the principle peak for a group of ions.

3.2 EXPERIMENTAL METHOD

During the course of the experiment the beam energy used was 1.35 MeV/u. This gave the experiment a centre-of-mass energy of 5.13 MeV. This energy was selected to compliment the energies investigated in previous experiments for the same reaction [4, 5], 1.513 MeV/u and 1.434 MeV/u.

The target was initially set to a pressure of 8.7 torr, although this varied slightly between runs to give an average value of 8.54 Torr. The pressure of the target is directly proportional to the density of target particles, so this value would impact the number of interactions occurring in the target. The pressure was chosen to maximise the overall recoil yield, thereby giving a more accurate count for yield per incident ion, necessary for calculating the cross section of the reaction.

Recoils exiting the target did so in a cone 0.00268 radians in diameter, well within the acceptance of the EMS, ± 20 milliradians. The combination of these two factors means that the EMS efficiency for the experiment is 100% for all practical purposes.

42 runs were conducted with the above settings after DRAGON had been recalibrated following preliminary test runs, for a total time on target of 1.24×10^5 seconds. From these runs the author selected 26 runs, totalling 8.5×10^4 seconds on target. Runs were excluded for a variety of factors, including the electric dipoles in the EMS switching off during the run, the run being used to check the Faraday cups, losing beam during the run or the run simply being too short to provide reliable results. For the runs that were selected time on target ranged between 1383 and 3396 seconds, with a median run time of 3389 seconds.

Chapter 4

ANALYSIS

As demonstrated earlier, cross section from a laboratory experiment can be determined by finding the ratio of experimental yield to target nuclei density. The yield per incident ion is calculated like so:

$$Y = \frac{N_R^{tot}}{N_b}, \quad (10)$$

where N_R^{tot} is the total number of recoils produced in a run and N_b is the total integrated beam on target for the duration of the run.

To calculate the actual number of recoils produced in an experiment, systematic inefficiencies must be factored in. In DRAGON's case the efficiencies that must be considered include: BGO detection efficiency, separator transmission efficiency, charge state fraction, detection deadtime (from the data acquisition system, DAQ), MCP transmission and detection efficiencies and DSSSD efficiency. Dividing the observed number of recoils from a run by these efficiencies results in the total number of reactions of interest:

$$N_R^{tot} = \frac{N_R^{det}}{\eta_{BGO}\eta_{EMS}\eta_{CSF}\eta_{LT}\eta_{MCP,T}\eta_{MCP,d}\eta_{DSSSD}}. \quad (11)$$

To find the total number of beam particles, the data gathered by the surface barrier detectors in the target must be normalised to give a total number of beam particles for the duration of each run.

4.1 BEAM NORMALISATION

Counts of elastically scattered beam particles are collected by the surface barrier detectors placed at angles of 30 and 57 degrees to the beam path within the gas target.

In order to calculate the total number of beam particles that impinged on the target during a run, a normalization factor must be applied to these counts to adjust the value based on the proportion of particles that would be elastically scattered. This factor is known as an R-factor and was defined in [18].

For a given time window, Δt , in which the beam intensity is constant, the R-factor is given by:

$$R = \frac{I/q}{e} \frac{\Delta t}{N_p E_{beam}^2 / P}, \quad (12)$$

where N_p is the number of elastically scattered particles within Δt , I is the beam current (measured by a Faraday cup ~2m upstream of the target), q is the charge state of the ions delivered as beam

by the ISAC accelerators (in this case ^{76}Se at 13+), E_{beam} is the incident beam energy (keV/u), P is the helium gas pressure (Torr), and $e = 1.602 \times 10^{-19}$ C.

When calculating the R-factor, the entire run is not used. The beam current is measured by putting Faraday cups into the beam line, thereby cutting it off from the target, so only the first and last two minutes of counts are considered satisfactorily recent so as to be relevant to beam current readings, which are taken immediately before and after each run. The R-factor is then calculated for each two-minute period at the beginning of each run and averaged with the corresponding R-factor for the end of the run, to give a normalisation factor for the entire run.

The total integrated beam on target for a given run is then calculated by multiplying the number of elastically scattered particles in a run by its R-factor, after the number of particles has been scaled by E_{beam}^2/P .

4.2 PARTICLE ID

Coincidences are particles detected by the DSSSD or MCP detectors whose timings coincide with a gamma-ray being detected by the BGO array near the target. As the reaction of interest produces a gamma as a product, the group of counts examined for the presence of recoils was immediately reduced to those which were also coincidences. This removes a large quantity of the background counts that would otherwise be present in the data.

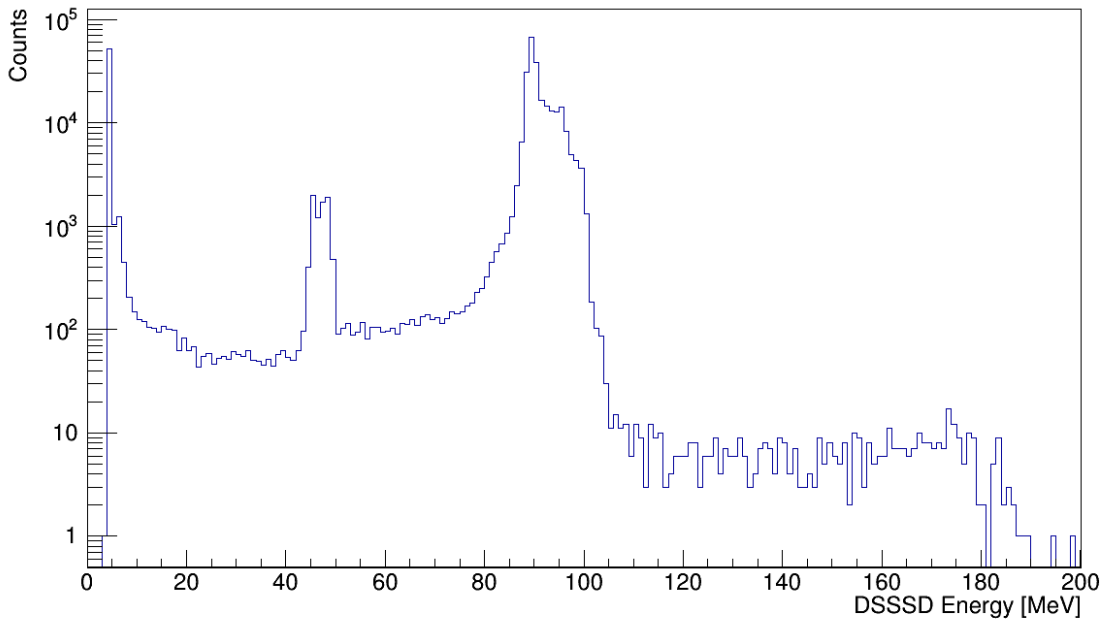


Figure 4.1: The DSSSD energy spectrum of DSSSD counts that registered with a corresponding count in the BGO array, coincidences. There is a significant peak that includes the expected energy of an ^{80}Kr recoil, 96 MeV, in its width.

Identifying recoil candidates from the coincidences registered by DRAGON meant finding a group of coincidences characteristically distinct from counts originating from leaky beam. The DSSSD energy was gated to only include counts greater than 70 MeV, isolating the peak seen in

the coincidence energy spectrum (see figure 4.1) and including a range of energies that captures the expected kinetic energy of the recoils, around 96 MeV.

Gamma rays released by the reaction of interest have a maximum possible energy of 10.12 MeV, which is the sum of the Q-value (the energy released by the reaction), 5.065 MeV, and the centre-of-mass energy of the reaction, 5.058 MeV. An upper energy gate was placed on BGO counts at 10.12 MeV to match this upper limit. A conservative lower energy gate was also placed on the BGO energy at 1.5 MeV. This was primarily to remove counts that happened to coincide with random background annihilations from particle-pairs, which typically produce low-energy gammas.

Finally, an adjustment was made to remove any counts present due to the effects of the pulser, a device that produces an artificial signal in the pre-amplification stage of data collection to make sure that the calibration of the electronics is not drifting.

Potential recoil events were first identified in analysis of the DSSSD energy vs MCP time-of-flight (MCP TOF, the time taken for a particle to travel between the MCP's two detector foils) coincidence spectrum. In the spectrum (see figure 4.2), two clear groups of counts are present, those with MCP TOFs of 3→20 ns, and those with MCP TOFs of 35→43 ns. Recoils are only to be expected around 39 ns, based on a classical approach to calculating the time-of-flight:

$$t_{MCP} = \frac{x_{MCP}}{v_R},$$

where t_{MCP} is the MCP TOF, x_{MCP} is the distance between the foils of the MCP and v_R is the velocity of the recoil. As such, the lower region of particles was disregarded and an MCP TOF gate

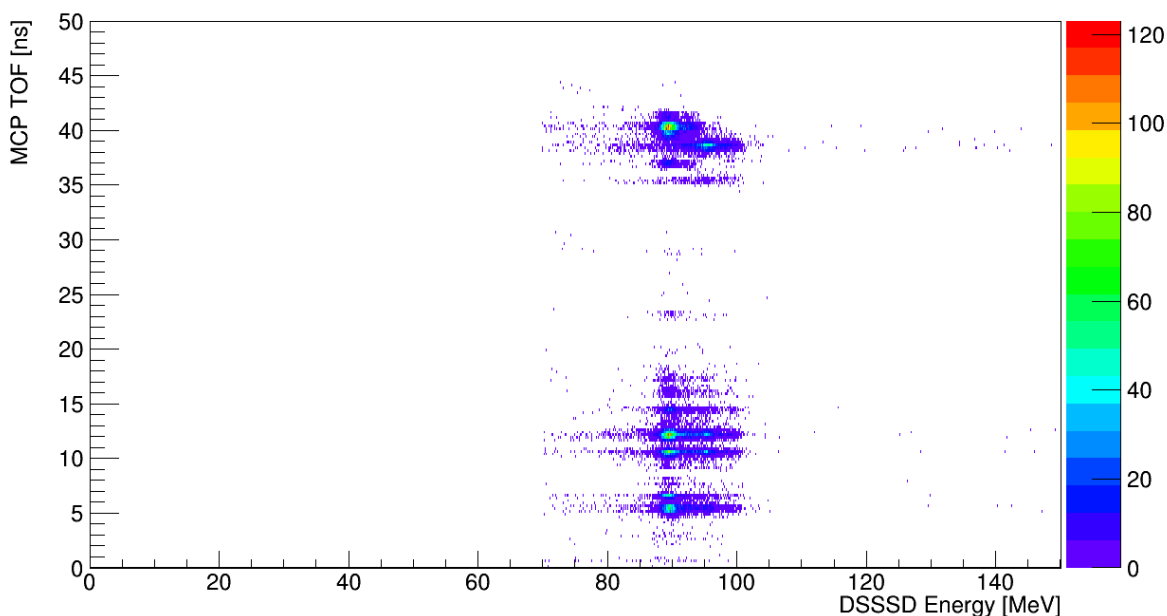


Figure 4.2: MCP TOF vs DSSSD coincidence spectrum gated on the DSSSD energy > 70 MeV, the BGO energy 1.5-10.12 MeV, and to remove the effects of the pulser. Two concentrations of counts can be seen, one with a range of MCP TOFs from 5→20 ns, and another at 35→43 ns. Recoils are expected at around 39 ns, so the lower group of counts was discounted from further analysis.

applied to include only counts falling in this upper, 35→43 ns region of the MCP TOF spectrum.

DRAGON filters particles based on their E/q ratio as they pass through the separator. This means that for reactions involving high-mass particles, particularly (α,γ) and (p,γ) reactions, there is often a lot of leaky beam detected by the DSSSD, as there are many charge states possible and the relative difference between the E/q ratio of unreacted beam particles and recoils is similar. In previous experiments featuring this reaction [4], experimenters were able to use dE vs dE information to distinguish between these groups, however as the experiment that is the focus of this paper did not make use of an IC, this was not possible with the current data set. This explains why the DSSSD spectrum, with the MCP TOF cut applied, features two clear peaks at different energies, one at 89 MeV and another at 95 MeV (see figure 4.3).

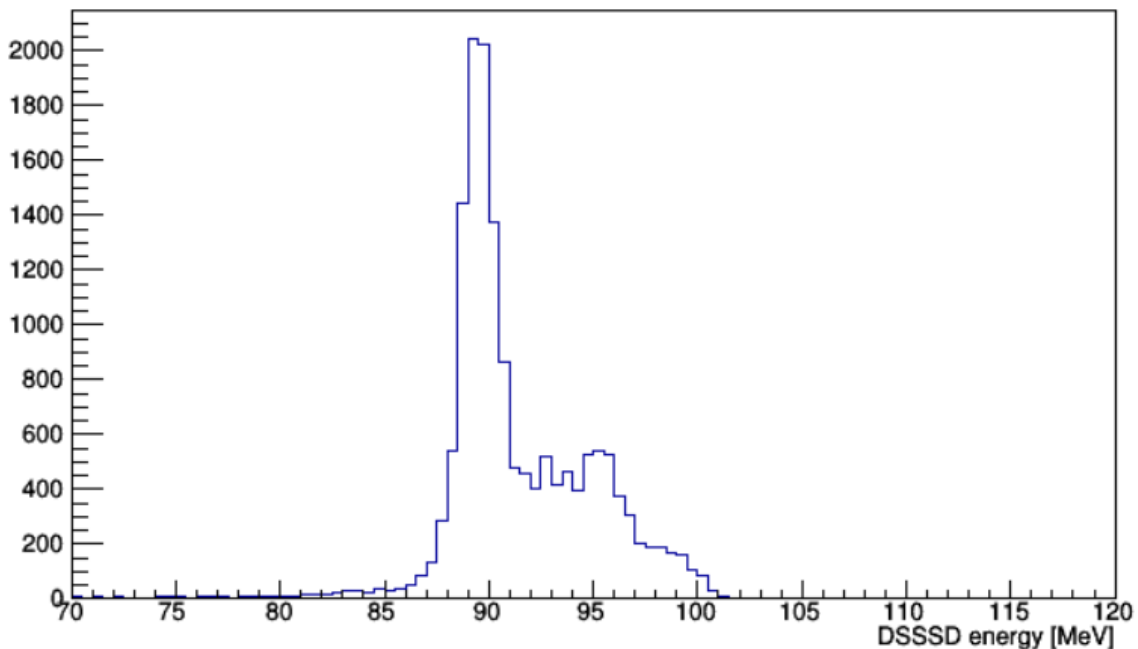


Figure 4.3: The DSSSD energy spectrum with an MCP cut of 35–43 ns applied. Evidence of two peaks can be seen, one at around 89 MeV and a smaller peak at around 95 MeV.

The expected energy for recoils, 96 MeV, correlates with the second of these two peaks, but whilst there is overlap between this peak and the one at 89 MeV, it is impossible to isolate these counts by simply placing a gate on the DSSSD energy. Instead, a DSSSD gate between 92 MeV and 102 MeV was used to see if a more distinct separation existed in another parameter, as demonstrated by the red lines featured on the DSSSD spectrum in Figure 4.3. When marked on the MCP-rf TOF vs separator time-of-flight (sepTOF, the time difference between the BGO array and the heavy ion detectors triggering, for a given event) in figure 4.4, the counts in this gate align strongly with the band of counts exhibiting an MCP-rf TOF of greater than 275 ns. The MCP-rf TOF is related to the time taken for a particle to travel from the beam-buncher that releases groups of particles into the beam, upstream of the target, to the MCP detector.

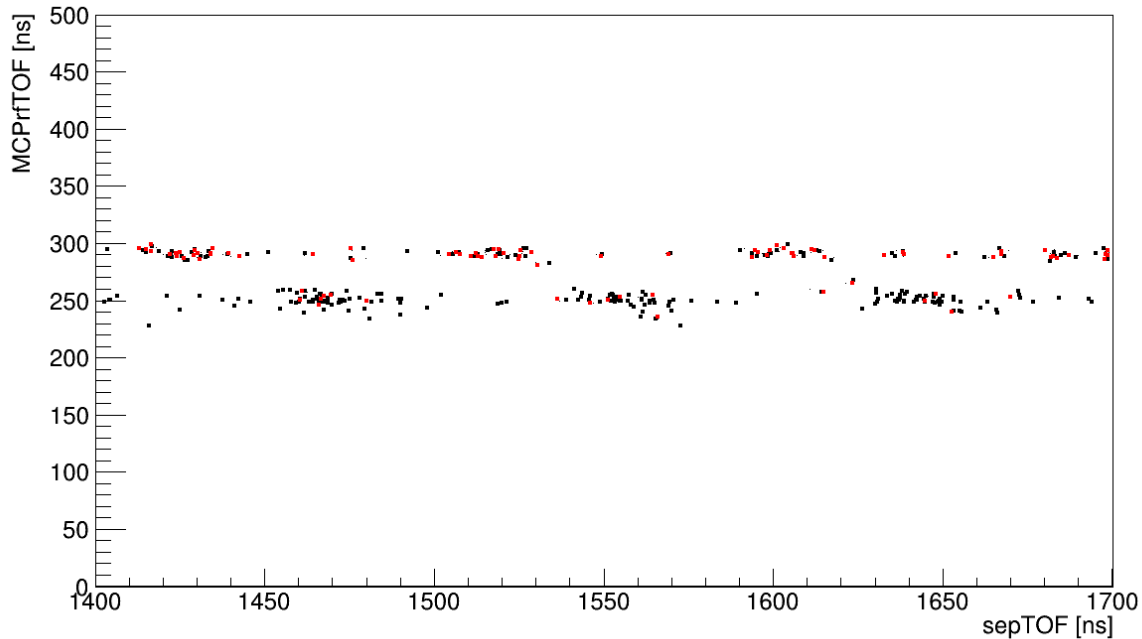


Figure 4.4: The MCP-rf TOF vs sepTOF spectrum for the 35→43 ns grouping of counts seen in Figure 4.2. The counts marked in red are those between 92-102 MeV, the region under the smaller peak in Figure 4.3. These counts have a clear correlation with the band of counts at MCP-rf TOF \approx 290-300 ns.

By gating on this band in the MCP-rf TOF, it was possible to extract the complete 95 MeV peak from the DSSSD spectrum with as few remnants from the 89 MeV peak as possible (see figure 4.5). It also had the effect of isolating a single peak from a pair in the MCP TOF spectrum, as shown by the red region in figure 4.6. The centroid of this peak is at a little over 39 ns, which falls within the range of expected MCP TOFs for recoils. Combined with the DSSSD energy of these counts, this appears to be compelling evidence for the existence of recoils within this group of counts.

Using the same method that was utilised to calculate an expected MCP TOF for the recoils, an expected sepTOF was calculated, giving an anticipated sepTOF_{recoil} of around 1530 ns. Figure 4.7 shows that with the current gating no distinct group of counts is present at this sepTOF, with a flat distribution of counts across the selected region. In fact, the regular grouping of counts in this coincidence spectrum suggests that these are mostly leaky beam events, which appear in bunches at regular intervals, due to their release by the buncher. These events can have sepTOFs that do not represent their actual time of flight because the value is determined with respect to the timestamp of a qualifying BGO interaction, in other words the timing of an unrelated event.

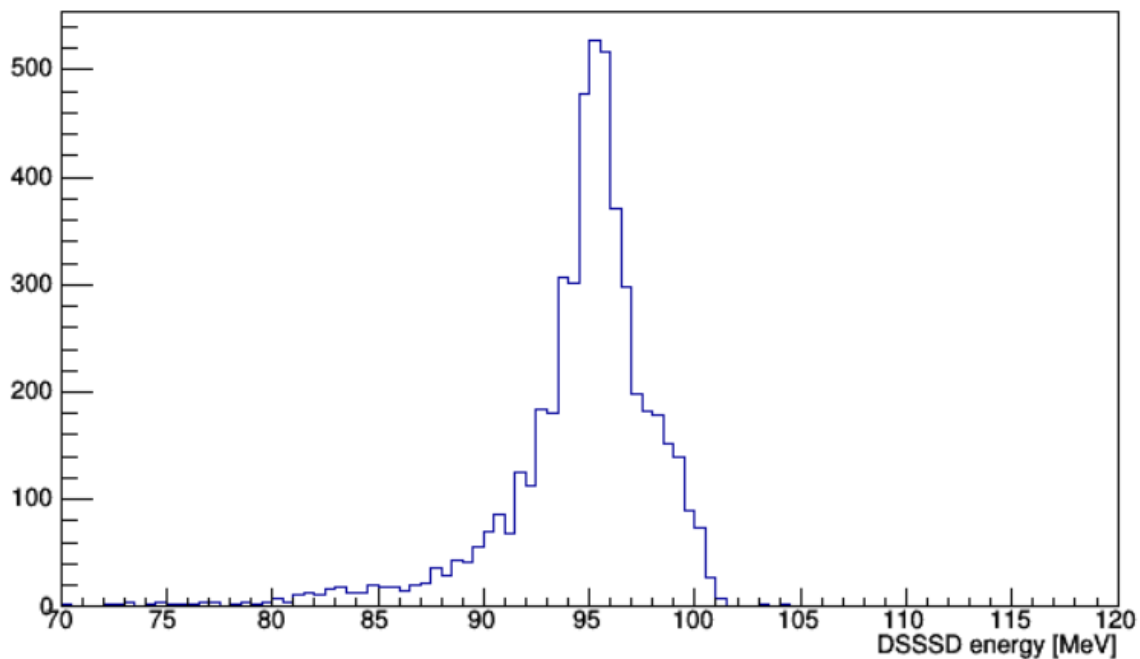


Figure 4.5: By limiting the MCP-rf TOF to values greater than 275 ns, the peak at 95 MeV can now be seen clearly in the DSSSD spectrum. This peak now appears to be completely free of counts from the other DSSSD peak that was present at 89 MeV. The peak is at an energy close to the anticipated DSSSD energy of an ^{80}Kr recoil, 96 MeV.

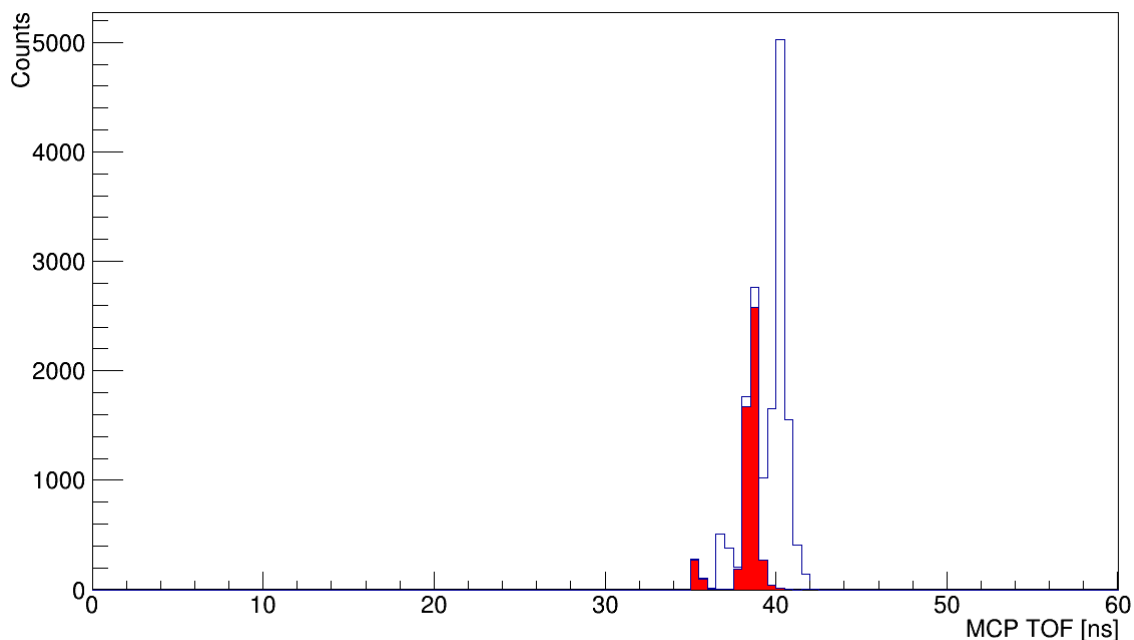


Figure 4.6: The MCP-TOF spectrum of the upper group of counts from Figure 4.2. The region highlighted in red is the counts where MCP-rf TOF > 275 ns. Aside from a few outliers, these counts form a peak around 39 ns, the same MCP TOF as expected for an ^{80}Kr recoil.

This does not mean there are no recoils present. It is possible that two groups of particles with

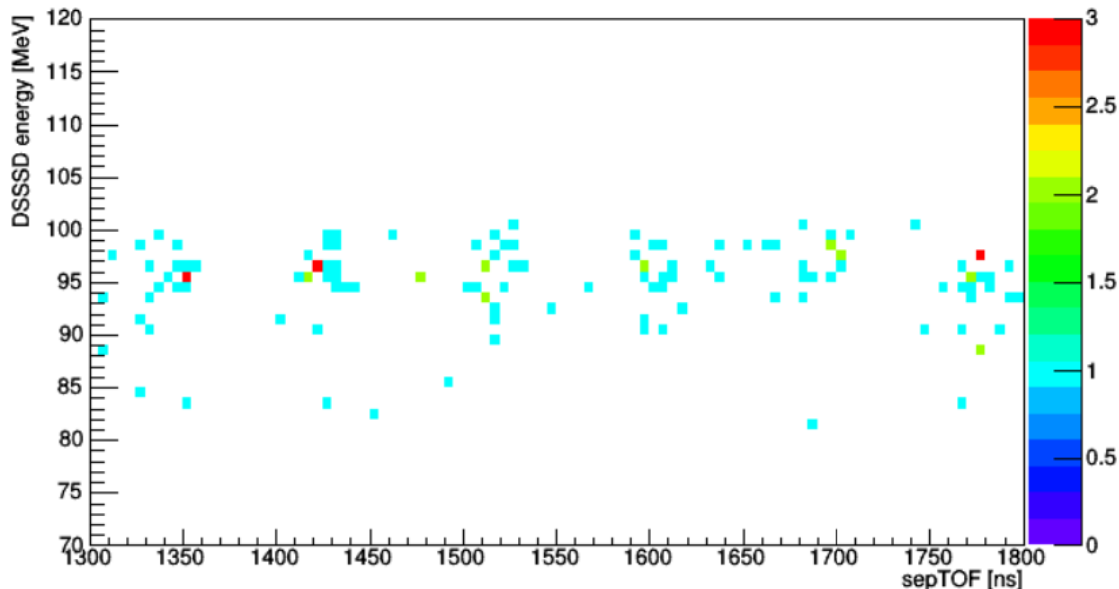


Figure 4.7: The sepTOF vs DSSSD energy spectrum with all previously mentioned cuts on DSSSD energy, BGO energy, MCP TOF and MCP-rf TOF. The expected sepTOF for recoils is 1530 ns, however no significant features or high-density groups of counts are present in this region of the spectrum.

similar physical properties were detected by DRAGON. The DSSSD detector (as described in section 3.1.7) features two layers of silicon strips for detecting the kinetic energy of particles that pass through the separator. These layers are orientated horizontally and vertically respectively, allowing a hit location for a given particle to be established. The hit pattern of the DSSSD was used to establish if two separate groupings of particles were registered by the heavy ion detectors. Figure 4.8 shows that the distribution of counts is largely homogenous aside from one extremely defined peak at the meeting point of strips 5 and 24 (5, 24). A cut was placed on this location to investigate whether this peak represented a significant sepTOF feature or revealed one in its absence.

Figure 4.9 shows that with a gate on the (5, 24) hit location for the DSSSD, there is little change in the distribution of counts on the sepTOF vs DSSSD energy spectrum. The distribution still shows the regular bunches of counts across the range of sepTOFs examined, with no additional intensity of counts around 1530 ns, as would be expected with the presence of recoils. The beam-like features of the counts visible here suggest much, if not all, of the counts present in this software gate represent leaky beam particles with similar physical attributes to those expected of recoils. With no additional ways to gate the data to find a group of counts with enough separation from these background counts to be reliably considered recoils, it must be concluded that either no recoils were detected in these experimental runs, or that any recoils present are obscured by the presence of large quantities of leaky beam particles.

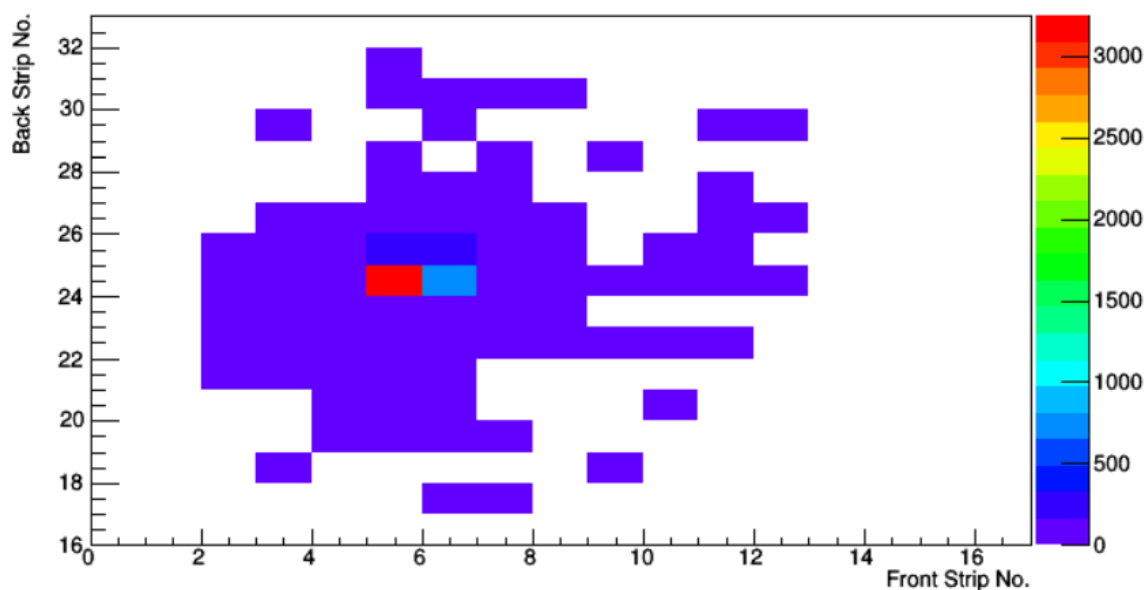


Figure 4.8: The DSSSD hit-pattern of the 95 MeV peak on the DSSSD energy spectrum. The distribution of counts is largely homogenous and thinly spread across much of the DSSSD, however there is one bin of counts with a significant number at the intersection between strips 5 and 24.

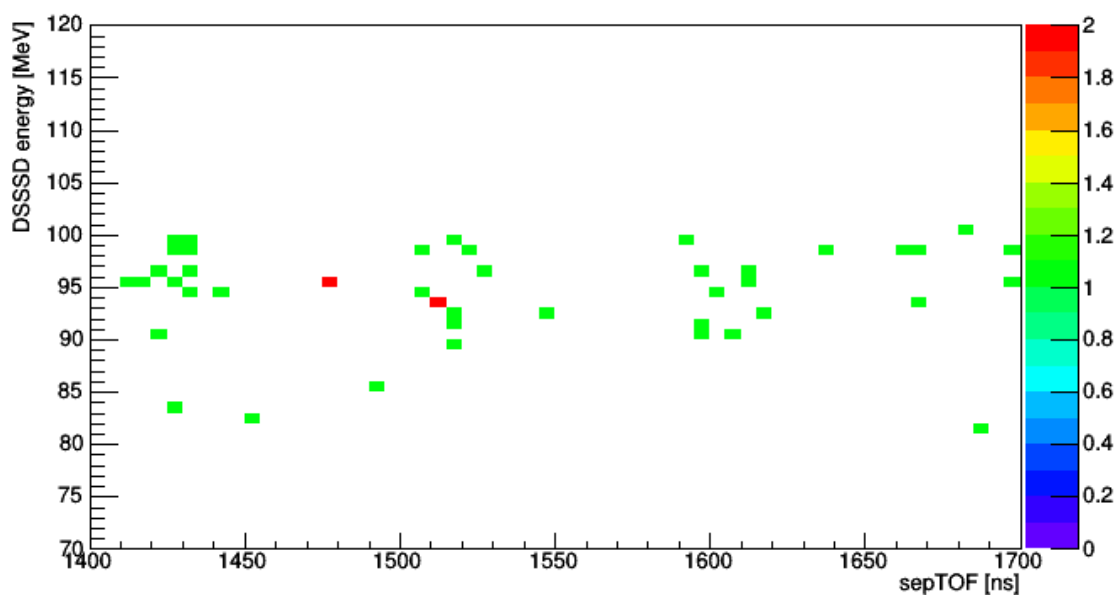


Figure 4.9: The sepTOF vs DSSSD energy spectrum for the counts in the bin (5, 24) from the DSSSD hit-pattern (Figure 4.8). The counts are distributed over the entire range of the spectrum and whilst their distribution is not completely even, there are no clear features to be seen that would suggest the presence of recoils. The counts are grouped at regular intervals, a characteristic of beam particles, which are bunched when they enter the beam.

Seeing as an exact number of recoils cannot be established, the next task is to attempt to estimate an upper limit for the number of recoils that could have been present in the data without

standing out from the background. The Rolke method [19] provides a route to calculating an upper limit for events in an experiment with a null result. In order to utilise this method, the average background for a typical region of data should be established. In this case, the “typical region” examined was data from the subset of counts included in the gate shown in Figure 4.9. In order avoid including potential recoils, the region around 1530 ns was excluded and five regular sepTOF intervals of data either side of this region were averaged to produce an expected background count. The width of this interval was chosen as 87 ns, to match the rf-frequency of the data, or the time-interval between beam-bunches being released by the buncher. Figure 4.10 shows this region of the sepTOF as a histogram, with each channel being an 87 ns interval. From this it was determined that the average background counts present in a typical region of the sepTOF, outside of the expected region for recoils, was 14.3 counts. At the 95% confidence interval, using the tables included in [20], this background gives an upper-limit on detected recoils, N_r^{det} , of 2 for the runs analysed.

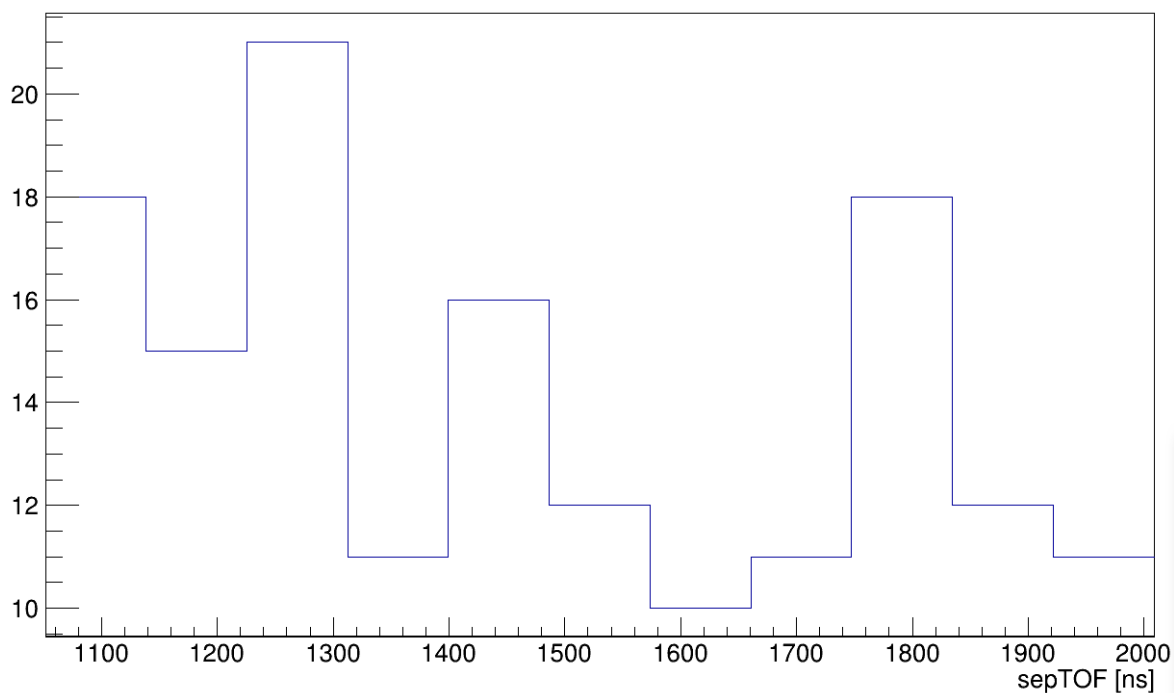


Figure 4.10: The sepTOF spectrum in the region surrounding 1530 ns, the anticipated sepTOF of recoils. The counts are binned at 87 ns intervals to match the intervals are which the buncher releases particles into the beamline.

4.3 CHARGE STATE DISTRIBUTION

Only one recoil charge state can be transmitted by DRAGON at a time because the recoil separator must be tuned to select for this particular state. This chosen state then only represents a fraction of the emitted recoils, and so the fraction of these compared to total recoils must be determined when calculating the actual number of recoils from the detected number.

In this experiment beam particles of ^{76}Se were delivered to the target in a charge state of 13+ and then the resulting recoils of ^{80}Kr , as well as any leaky beam were passed through a charge state booster to get the charge up to a value high enough to be bent by the magnetic and electric dipoles.

Since the separator was originally built to handle recoils of a much lower mass, a high charge state is required in order for the separator to select heavy ion recoils such as ^{80}Kr , and even then, only a small percentage of recoils have sufficient charge to be reliably guided by the separator.

In this case, a charge state of 25+ was selected for the recoils. Previous work done on this reaction involved modelling the CSD at a range of energies, which can be seen in figure 4.11. For the beam energy of this experiment, 1.35 MeV/u, this charge state represents 2.5% of the total expected recoils. Uncertainty arising from the fit was considered to be the average displacement from the experimental points, weighted by the uncertainty on those points [4], giving a charge state fraction (CSF) of $\eta_{\text{CSF}} = 2.5 \pm 0.06\%$.

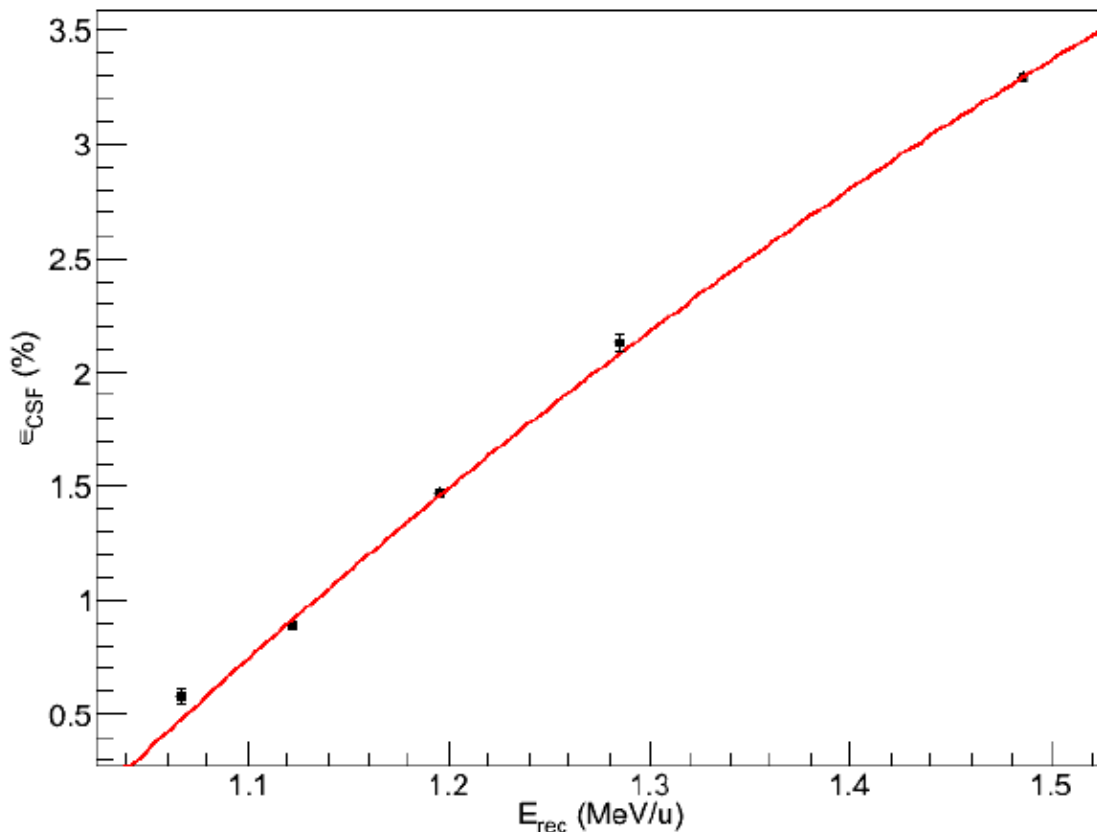


Figure 4.11: Measured charge state fractions of ^{80}Kr , in the 25+ charge state, for a variety of energies. A second order polynomial fit is shown in red. Taken from [4].

4.4 EFFICIENCIES

At every stage of transmission, detection and data acquisition in this experiment existed the possibility that real recoils were not transmitted or detected. Therefore, the final number of counts detected by DRAGON will be lower than the actual number of recoils produced in the experiment. The efficiencies that need to be accounted for to find this true number of recoils were listed in the introduction to this section. This subsection will explore each of these efficiencies and discuss how the values used in this analysis were arrived at.

4.4.1 Separator Efficiency

This is the efficiency with which products of a radiative capture reaction, after leaving the gas

target, make it through the separator. For this experiment it was determined that this value is ~ 1 , as the reaction cone angle is relatively small (~ 2 milliradians) compared to DRAGON's acceptance angle (20 milliradians).

4.4.2 Live Time Efficiency

During the running of the experiment, the data acquisition unit (DAQ), records information coming in from the various parts of DRAGON and the DSSSD detector. This efficiency represents the portion of time the experiment was running in which experimental data, was able to be processed by DAQ.

η_{LT} can be calculated using the ROOT-based DRAGON analysis software, by comparing the number of data triggers presented to the number of data triggers required. After chaining together all the runs used in this analysis, it was determined that the live time efficiency was 87.9%, where the uncertainty is statistically negligible ($\pm 4.4 \times 10^{-5}$) and determined from the uncertainty in the quantity of triggers.

4.4.3 MCP Transmission Efficiency

The MCP transmission efficiency represents the proportion of particles that are transmitted through both sheets of the multi-channel plate detector, as opposed to passing through one or neither before being stopped. This can be measured by comparing attenuated beam runs with the MCP grids in place to those with the grids removed, however this data set featured only one attenuated beam run, so the author was unable to calculate a transmission efficiency for this experiment. However, previous experiments testing the same reaction at DRAGON used the same the same MCP setup [4], for which an MCP transmission efficiency, $\eta_{MCP,t}$, was calculated from the average 29 such runs, with MCP alternately in and out of the beamline. This returned an $\eta_{MCP,t} = 66.5 \pm 2.2\%$ [4], where uncertainty stems from the standard error in the mean for multiple measurements.

This is a lower efficiency than was measured for the same equipment in [21], $76.9\% \pm 0.6$, which was the previously accepted standard. This is owing to the replacement of the final MCP grid with one featuring a thicker wire mesh. This mesh was also the one in use when the experimental runs in this data set were performed.

4.4.4 MCP Detections Efficiency and DSSSD Efficiency

The MCP detection efficiency and the DSSSD efficiency can be characterised by utilising data from attenuated beam runs. These efficiencies share a relationship with the total number of incoming beam particles. This relationship is shown in the following equations:

$$N_{DSSSD} = N_{tot} \cdot \eta_{DSSSD} \cdot \eta_{MCP,t}, \quad (16)$$

$$N_{MCP,d} = N_{tot} \cdot \eta_{MCP,d} \cdot \eta_{MCP,t}^* \quad (17)$$

where N_{tot} is the total number of incoming beam particles and N_{DSSSD} , $N_{MCP,d}$, and $N_{DSSSD, MCP,d}$ are the number of events in the DSSSD spectrum, in the MCP spectrum, and in the DSSSD *and* MCP spectra, respectively. η_{DSSSD} is the DSSSD efficiency, which here is nominally taken to be 96.15% [22], $\eta_{MCP,d}$ is the MCP detection efficiency, $\eta_{MCP,t}$ is the MCP

transmission efficiency, $66.5 \pm 2.2\%$, $\eta_{MCP,t}^*$ is a modified MCP transmission efficiency that takes into account that a particle does not have to pass through the final MCP mesh to record an MCP TOF. This means that $\eta_{MCP,t}^* = \eta_{MCP,t} / \eta_{MCP,t}^f$, where $\eta_{MCP,t}^f$ is the transmission efficiency of MCP1 (the final MCP mesh).

Equation 17, can then be rewritten as:

$$N_{MCP,d} = N_{tot} \cdot \eta_{MCP,d} \cdot \frac{\eta_{MCP,t}^*}{\eta_{MCP,t}^f}. \quad (18)$$

The number of simultaneous hits on the DSSSD and MCP can then be given by:

$$N_{DSSSD, MCP,d} = N_{tot} \cdot \eta_{DSSSD} \cdot \eta_{MCP,d} \cdot \eta_{MCP,t}^f. \quad (19)$$

The MCP and DSSSD detection efficiencies can then be calculated by dividing equation 19 by equations 16 and 18 respectively:

$$\frac{N_{DSSSD, MCP,d}}{N_{DSSSD}} = \eta_{MCP,d}, \quad (20)$$

and:

$$\frac{N_{DSSSD, MCP,d}}{N_{MCP,d}} = \eta_{MCP,t}^f \cdot \eta_{DSSSD}. \quad (21)$$

The author used attenuated run 4667 to characterise $\eta_{MCP,d}$ and η_{DSSSD} . After examining the uncut MCP TOF and DSSSD spectra for the run (fig 4.12), cuts were made on an MCP TOF range of $35 \rightarrow 42$ ns, and above a DSSSD energy of 70 MeV, each to remove suspected background counts based on the likely locations of beam counts in a normal experimental run.

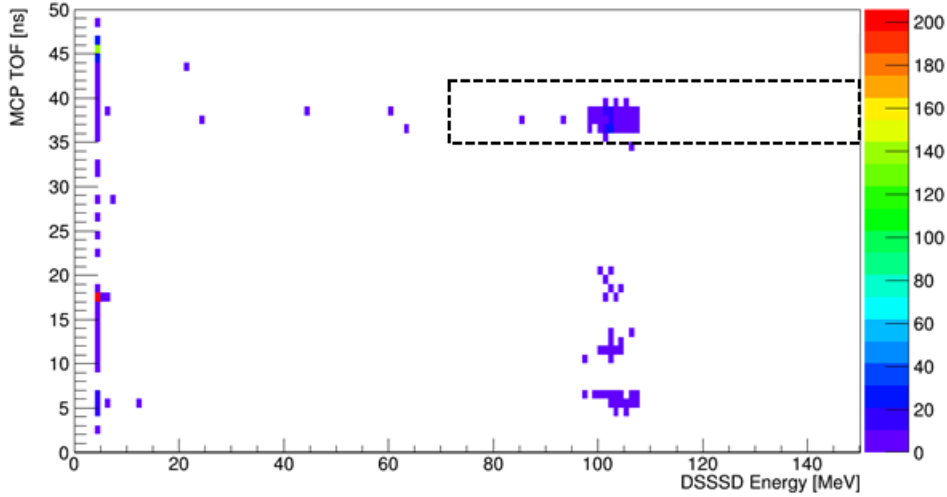


Figure 4.12: The MCP time of flight plotted against the DSSSD energy of singles events for the attenuated beam run, 4667. It was decided that to determine the efficiency of the MCP detector and the DSSSD, cuts would be applied to the MCP spectrum based on the DSSSD (DSSSD energy > 70 MeV), and vice versa (MCP TOF $35 \rightarrow 45$ ns), this region being marked out by the dashed black box. These gates were based on the expectations held when looking for counts of beam or recoil in a full experimental run. All other counts were discounted as anomalous.

Final counts obtained were $N_{\text{DSSSD}} = 186 \pm 14$, $N_{\text{MCP},d} = 198 \pm 14$ and $N_{\text{DSSSD},\text{MCP}} = 141 \pm 12$ (where the uncertainties are all obtained from the standard uncertainty for a number of counts), giving final efficiencies of $\eta_{\text{DSSSD}} = 96.15 \pm 10.6\%$ (where $\eta_{\text{MCP},t}^f = 74.1\%$) and $\eta_{\text{MCP},d} = 75.8 \pm 8.5\%$, where the uncertainties stem from uncertainty about the number of counts registered.

4.4.5 BGO efficiency

In the above analysis of the data gathered in this experiment, a coincidence gate was used in filtering for recoils. This gate eliminated singles counts that did not have an associated count on the BGO array. It is then necessary to account for the detection efficiency of this array when calculating an overall efficiency for the experiment.

The efficiency of the BGO in this scenario is in no small part governed by the level scheme of the compound nucleus, ^{80}Kr [4]. Whilst work has been done to characterise this level scheme [23], this has only been achieved for a small group of high spin states and a full decay scheme is not yet known.

In order to calculate the efficiency in the absence of a known decay scheme, a simulation was performed, testing a variety of gamma-cascade schemes, to determine a range of possible efficiencies [4]. This simulation involved a 3D model of the array and was performed in the Geant4 software, taking into account a number of factors present in the real experiment, such as the 1.5 MeV lower limit on detection, designed to eliminate the effects of random gamma annihilations [4].

2754 unique cascade combinations were run in the simulation, giving an efficiency range of 65% -> 95% [4]. The higher efficiency cascades featured many gamma events above the BGO-threshold, whereas lower events featured as few as one. This gives a η_{BGO} of $80 \pm 10\%$, calculated by averaging the upper and lower limits of the range of efficiencies generated, with the standard deviation of the entire group of values taken as the uncertainty, assuming all values are equally likely [4]. Adding to this there is a small systematic uncertainty of 6%, stemming from the discrepancy between this simulation and an experimental test of the BGO efficiency which utilised a $^{244}\text{Cm}^{13}\text{C}$ target [4]. Factoring this in, a final BGO efficiency of $80 \pm 11\%$ is achieved.

4.4.6 Final Coincidences Efficiency

Efficiency	Value (%)	Error (%)
η_{EMS}	100.0	1.0×10^{-3}
η_{CSF}	2.5	6.0×10^{-3}
η_{LT}	87.9	4.4×10^{-5}
$\eta_{\text{MCP},T}$	66.5	2.2
$\eta_{\text{MCP},d}$	75.8	8.5
η_{DSSSD}	96.2	10.6
η_{BGO}	80.0	11.0

Table 4.1: The efficiencies required to calculate the final coincidence detection efficiency, η_{coinc} , along with the associated uncertainty values.

Having calculated all the individual efficiencies necessary to determine an accurate value for the number of recoils in the experiment, it is now possible to combine these into one final coincidences efficiency. Using the values from table 4.1, the coincidences efficiency, η_{coinc} is:

$$\eta_{coinc} = 0.85 \pm 0.18\%.$$

where the uncertainty in the efficiency was calculated by taking the square root of the sum of the squared ratios between error and associated efficiency, finding its product with the coincidence efficiency.

Taking the upper limit established for the number of recoils present in the final data-cut in Section 4.3, an upper limit on the number of recoils after accounting for efficiencies was calculated and is listed in Table 4.2.

N_{data}	$N_{recoils}$
2	235

Table 4.2: N_{data} is the upper limit on the number of recoils present in the final gate applied to the data set in Section 4.3 after utilising the Rolke method. Accounting for the efficiencies of the various components of DRAGON yields $N_{recoils}$, which is the upper limit on the number of recoils produced across all runs in the data set. The uncertainty for this value is based on the RMS of the error in the final coincidences efficiency.

Chapter 5

RESULTS AND DISCUSSION

An experimental cross section was calculated for the $^{76}\text{Se}(\alpha,\gamma)^{80}\text{Kr}$ reaction at a beam energy of 1.35 MeV/u, using data gathered from experimental runs performed under the setup described in section 3.2, which was analysed for evidence of recoils as detailed in section 4.

Upon analysis of the data, no group of counts could be found that was characteristically distinct enough to be sure that they were recoils. Whilst a group of particles exhibited properties similar to those expected of the recoils: a DSSSD energy of around 96 MeV, an MCP TOF of around 39 ns, and a tight grouping on the DSSSD hit-pattern; the sepTOF spectrum continued to show no region in which counts were particularly dense (see figure 4.9). This was particularly clear in the region around 1530 ns, where classical estimations of the recoils' separator time-of-flight would have placed them. Due to the similar E/q ratio of beam and recoil particles, it was concluded that a large proportion of the counts in this spectrum represented leaky beam, and likely rendered any attempts to identify the small anticipated number of recoils futile

As it was determined that no recoils could be extracted from the background, the Rolke method was employed to estimate an upper bound on the number of recoils present, based on the amount of background present in the sepTOF region surrounding the sepTOF where recoils would have been expected. After accounting for the efficiency of DRAGON's systems at detecting coincidences by adjusting the upper-recoil limit, a cross section was calculated using (6) yielding a final, upper limit, cross section of $0.021 \pm 0.004 \mu\text{b}$ (see table 5.1 for full numbers). The uncertainty in this value was calculated from the counting errors of the number of recoils, beam particles and target particles.

E_b (MeV/u)	E_{CM} (MeV)	σ_{exp} (μb)	σ_{SM} (μb)	N_R^{tot}
1.35 ± 0.003	$5.058 \rightarrow 5.13 \pm 0.012$	0.021	0.23	235

Table 5.1: The calculated upper-limit of the experimental cross section (σ_{exp}), from beam energy (E_b), which corresponds to the centre of mass energy (E_{CM}). Displayed alongside the theoretical cross section (σ_{SM}), which was generated by extrapolating SMARAGD data from [5]. Also shown is the upper-limit on recoils present in the software gate (N_R^{tot}).

This value is around $1/10^{\text{th}}$ of the cross section predicted by the SMARAGD model, $0.23 \mu\text{b}$. If the SMARAGD model was accurate at this centre-of-mass energy, then 22 recoil counts could have been expected within the region analysed in Section 4.2, which given the sparseness of counts in figure 4.9 would surely have appeared as a clear feature above background. In comparison to the other models seen in figure 5.1, the experimental upper-limit for the cross section is lower than all of the theoretical predictions. This in contrast to the cross sections calculated for this reaction at higher energies (see figure 5.1 and figure 1.4), which are close to the fit provided by SMARAGD [4, 5]. Of all the models, TALYS αOMP5 is in best agreement with the experimental result, with a cross section of $0.041 \mu\text{b}$, equivalent to around 4 counts being present in the data, although this does not hold true at higher energies

Given that this experiment has only produced an upper-limit on the cross section, and that there

is such a disparity between this value and the cross section anticipated by theoretical models, there would be value in additional beam time to see if producing a greater quantity of recoils would allow a value for the cross section to be derived directly from visible recoil counts, rather than extrapolating from the amount of background. This could be achieved by having more time on target; the runs analysed here amounted to 85,082 seconds of beam on target. For 20 counts, this time would need to be 850,820 seconds at the same beam intensity, but this time could be decreased by increasing either the target pressure or the beam intensity, thereby increasing the expected reaction rate. Even ignoring these latter options, the experiment could be completed within two weeks if the beam ran 24-hours a day, even accounting for setup time, calibration and runs not fit for analysis purposes. Another alternative would be to repeat the experiment but to utilise the Ion Chamber in DRAGON's hybrid setup, as opposed to the DSSSD. ^{80}Kr recoils have

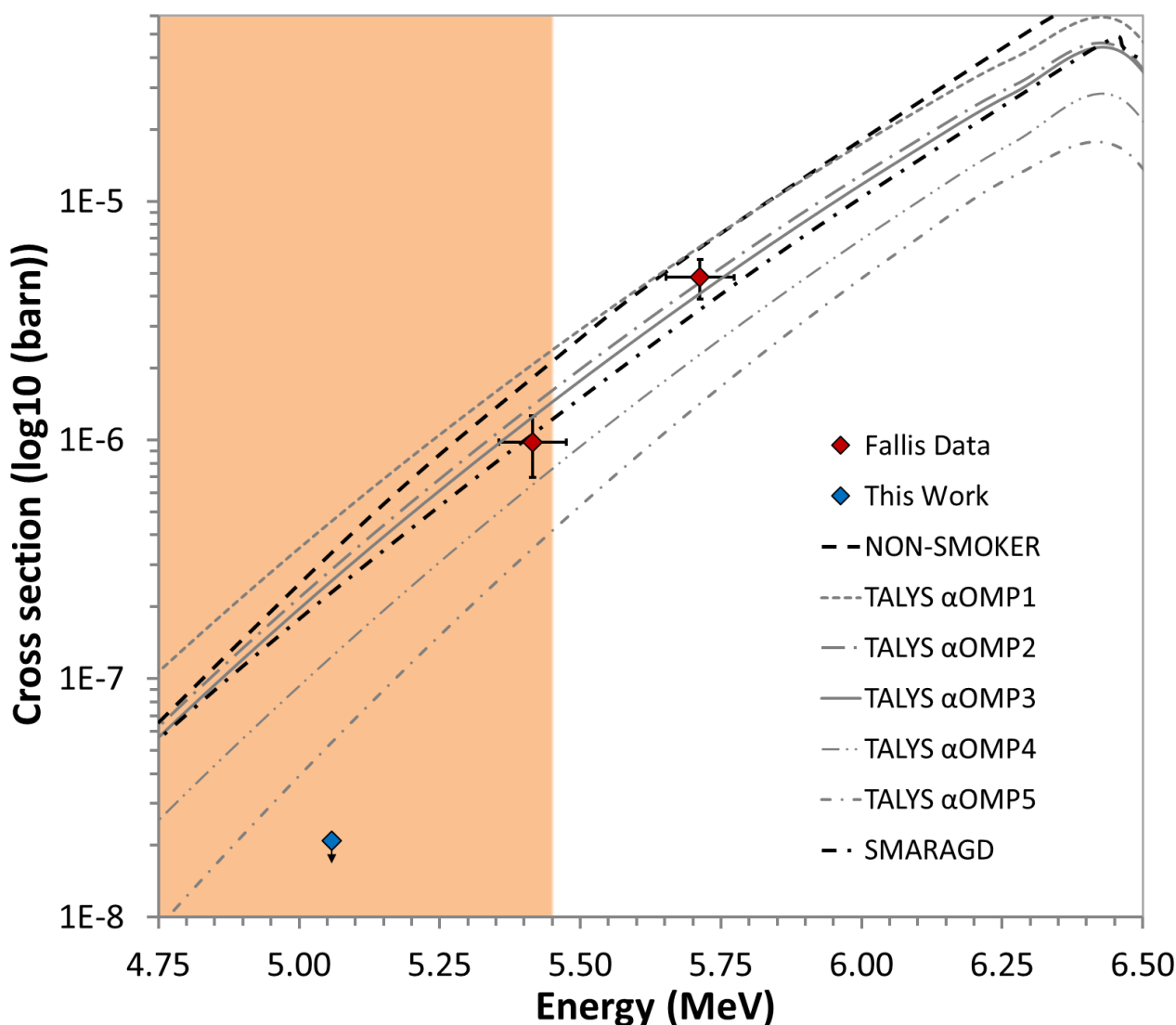


Figure 5.1: The calculated upper-limit of the experimental cross section, in blue, is compared to the cross sections determined by [4, 5], in red (also seen in figure 1.4), and the models featured in [5], including the SMARAGD model. The experimental value is a factor-of-10 less than the SMARAGD cross section at this energy. The orange region indicates the 1.7GK Gamow window.

been more readily identified amongst background in the past, when making use of IC-data [4].

Overall, a lower cross section than expected does have ramifications for the aims of this experiment presented at the outset. Considered alongside the results from [4], it could be interpreted that in lower energy regions, the cross section falls away from the values derived from the current theoretical models. If the cross section is indeed lower than expected, this would suggest that in this energy region, the competing (γ,p) and (γ,n) reactions would likely dominate the reverse kinematic $^{80}\text{Kr}(\gamma,\alpha)^{76}\text{Se}$ reaction. The effect of this is that the production of the ^{78}Kr p-nuclide would be higher than suggested by the SMARAGD cross section for the investigated reaction. So, even though, only an upper-limit could be established for the cross section of this reaction, it can be used to further understanding of reaction rates in this stellar environment and improve computational models of stellar explosions.

Chapter 6

CONCLUSION

To better understand the processes that lead to the production of the p-nuclides, an experiment was conducted to measure the cross section of the $^{76}\text{Se}(\alpha, \gamma)^{80}\text{Kr}$ reaction. This reaction is the time-reversed form of the $^{80}\text{Kr}(\gamma, \alpha)^{76}\text{Se}$ reaction, which occurs at a branching point. Here it competes with (γ, n) and (γ, p) reactions, the latter of which is responsible for the production of the p-nuclide ^{78}Kr . Should $^{80}\text{Kr}(\gamma, \alpha)^{76}\text{Se}$ be found to have a greater reaction-rate at a given energy than this (γ, p) reaction then ^{78}Kr could be expected to have a reduced abundance in such an environment. By determining a cross section for $^{76}\text{Se}(\alpha, \gamma)^{80}\text{Kr}$, the cross section and therefore the reaction-rate of $^{80}\text{Kr}(\gamma, \alpha)^{76}\text{Se}$ can eventually be inferred, allowing for a more complete understanding of ^{78}Kr production rates.

The experiment was performed by projecting a charged ion beam of ^{76}Se at a beam-energy of 1.35 MeV/u (an as yet unobserved beam-energy) onto a windowless gas target containing Helium. Here successful reactions produced a gamma, whose energy was registered by the BGO detector array (if detected), and a recoil. Recoils then had their charge boosted by a booster-foil to give them sufficient charge to make it through DRAGON's EMS, where they were separated from leaky beam particles, before being detected by an MCP-detector and a DSSSD.

In the process of particle-ID, counts that did not have a coincident gamma count from the BGO were discounted to reduce the amount of leaky beam counts in the data. Cuts were made on the DSSSD energy, MCP-TOF, MCP-rf TOF and BGO energy to try and find a group of counts characteristically distinct enough from the large quantities of background to say with confidence that they represented "real" recoils. It was determined from the profile of the separator time-of-flight spectrum, that counts appeared at no greater density at the expected time-of-flight for recoils than that any other region in the spectrum. Given the presence of significant amounts of leaky beam counts, it was concluded that even if recoils were present in the data, it would be impossible to identify them with the information available.

Without recourse to identify recoils in the dataset, the Rolke method was employed to determine an upper limit on the number of recoils present in the data based on the amount of background counts in that region of the sepTOF. This value was then divided by an overall coincidence efficiency, describing the overall efficiency of DRAGON's components at detecting and transmitting coincidences, to produce an upper-limit on the number of recoils produced across the total run time of the experiment. The number of beam particles on target and the number of target particles in the beam-line were calculated, the former from elastic-scattering data collected by surface-barrier detectors positioned at an angle to the target, the latter from pressure data collected during runs. These values along with the upper-limit on recoils produced were utilised to calculate a cross section for the reaction (albeit an upper-limit on the cross section), $\sigma_{\text{exp}} = 0.021 \mu\text{b}$.

Compared to theoretically derived cross sections at this energy, the value determined for the experiment was small, being ten times smaller than the value predicted by the SMARAGD model.

This is unlike the cross sections observed for the same reaction at higher energies, which were in good agreement with the modelled cross sections. It could mean that the models in question are limited in their predictive power at lower energies with respect to this reaction. To confirm the result of this experiment, the author recommends additional runtime using DRAGON, this time making use of the available Ion Chamber, which has been shown to be more effective at allowing recoils to be identified in spite of heavy background than when using the DSSSD. This experiment highlights the DSSSD's limited capacity for particle ID in this mass-region.

Regardless, the lower upper-limit on the cross section infers a lower upper-limit on the reaction rate not only for this reaction but for the related $^{80}\text{Kr}(\gamma,\alpha)^{76}\text{Se}$ reaction. This lower reaction rate implies a higher production rate of ^{78}Kr than was first suggested by theoretical models such as SMARAGD, at a centre-of-mass energy of $5.06 \rightarrow 5.13$ MeV.

Bibliography

- [1] T. Rauscher, N. Dauphas, I. Dillmann, C. Fröhlich, Z. Fülöp and G. Gyürky, "Constraining the astrophysical origin of the p-nuclei through nuclear physics and meteoritic data," *Reports on Progress in Physics*, vol. 76, p. 066201, 5 2013.
- [2] T. Rauscher, "Branchings in the process path revisited," *Physical Review C*, vol. 73, 1 2006.
- [3] A. M. Laird, J. Fallis, B. R. Fulton, S. P. Fox, C. Ruiz, A. S. Murphy and D. A. Hutcheon, A Direct Measurement of the $^{76}\text{Se}(\alpha, g)^{80}\text{Kr}$ Reaction, 2010, (EEC Proposal, TRIUMF, EEC Meeting: 201012S) Experiment No.: S1318.
- [4] C. Akers, "Radiative Capture Measurements of Astrophysically Important Reactions Using the DRAGON Separator," 2014 (University of York). Online: <http://etheses.whiterose.ac.uk/id/eprint/7879>
- [5] J. Fallis, C. Akers, A. M. Laird, A. Spyrou, G. Christian, D. Connolly, B. Davids, U. Hager, D. A. Hutcheon, P. O'Malley, S. J. Quinn, J. E. Riley, A. Rojas and C. Ruiz, "First measurement of a p process reaction in inverse kinematics at astrophysical energies: $^{76}\text{Se}(\alpha, \gamma)^{80}\text{Kr}$ ", 2016 (in preparation)
- [6] T. Rauscher, "THE PATH TO IMPROVED REACTION RATES FOR ASTROPHYSICS," *International Journal of Modern Physics E*, vol. 20, pp. 1071-1169, 5 2011.
- [7] nuclear-power.net, What is Nuclear Resonance – Compound Nucleus. Online: <https://www.nuclear-power.net/nuclear-power/reactor-physics/nuclear-engineering-fundamentals/neutron-nuclear-reactions/compound-nucleus-reactions/what-is-nuclear-resonance-compound-nucleus/>. Date accessed: 06/12/2018
- [8] C. E. Rolfs and W. S. Rodney, *Cauldrons in the cosmos: Nuclear astrophysics* 1st ed., 1988, University of Chicago Press (Chicago), p580.
- [9] C. Iliadis, *Nuclear Physics of Stars* 2nd ed., Wiley VCH Verlag GmbH, 2015, p76.
- [10] D. A. Hutcheon, S. Bishop, L. Buchmann, M. L. Chatterjee, A. A. Chen, J. M. DAuria, S. Engel, D. Gigliotti, U. Greife, D. Hunter, A. Hussein, C. C. Jewett, N. Khan, M. Lamey, A. M. Laird, W. Liu, A. Olin, D. Ottewell, J. G. Rogers, G. Roy, H. Sprenger and C. Wrede, "The DRAGON facility for nuclear astrophysics at TRIUMF-ISAC: design, construction and operation," *Nuclear Instruments and Methods in Physics Research Section A: Accelerators, Spectrometers, Detectors and Associated Equipment*, vol. 498, pp. 190-210, 2 2003.
- [11] L. Bonnet, M. Frederic, P. Leleux, I. Licot and P. Lipnik, "Optimization of NaI(Tl) detector performance in high background counting rate environments," *Nuclear Instruments and Methods in Physics Research Section A: Accelerators, Spectrometers, Detectors and Associated Equipment*, vol. 292, pp. 343-350, 7 1990.
- [12] J. G. Rogers and C. J. Batty, "Afterglow in LSO and its possible effect on energy resolution," *IEEE Transactions on Nuclear Science*, vol. 47, pp. 438-445, 4 2000.

- [13] O. H. Nestor and C. Y. Huang, "Bismuth Germanate: A High-Z Gamma-Ray and Charged Particle Detector," *IEEE Transactions on Nuclear Science*, vol. 22, pp. 68-71, 1975.
- [14] A. Olin, S. Bishop, L. Buchmann, M. L. Chatterjee, A. Chen, J. M. DAuria, S. Engel, D. Gigliotti, U. Greife, D. Hunter, A. Hussein, D. Hutcheon, C. Jewett, J. King, S. Kubono, M. Lamey, A. M. Laird, R. Lewis, W. Liu, S. Michimasa, D. Ottewell, P. Parker, J. Rogers, F. Strieder and C. Wrede, "Nuclear astrophysics at ISAC with DRAGON: Initial studies," *Nuclear Physics A*, vol. 721, pp. C1019--C1023, 6 2003.
- [15] C. Vockenhuber, C. O. Ouellet, L. Buchmann, J. Caggiano, A. A. Chen, J. M. D'Auria, D. Frekers, A. Hussein, D. A. Hutcheon, W. Kutschera, K. Jayamanna, D. Ottewell, M. Paul, J. Pearson, C. Ruiz, G. Ruprecht, M. Trinczek and A. Wallner, "The $^{40}\text{Ca}(,)^{44}\text{Ti}$ reaction at DRAGON," *Nuclear Instruments and Methods in Physics Research Section B: Beam Interactions with Materials and Atoms*, vol. 259, pp. 688-693, 6 2007.
- [16] A. Simon, J. Fallis, A. Spyrou, A. M. Laird, C. Ruiz, L. Buchmann, B. R. Fulton, D. Hutcheon, L. Martin, D. Ottewell and A. Rojas, "Radiative capture reactions with heavy beams: extending the capabilities of DRAGON," *The European Physical Journal A*, vol. 49, 5 2013.
- [17] S. Engel, D. Hutcheon, S. Bishop, L. Buchmann, J. Caggiano, M. L. Chatterjee, A. A. Chen, J. D'Auria, D. Gigliotti, U. Greife, D. Hunter, A. Hussein, C. C. Jewett, A. M. Laird, M. Lamey, W. Liu, A. Olin, D. Ottewell, J. Pearson, C. Ruiz, G. Ruprecht, M. Trinczek, C. Vockenhuber and C. Wrede, "Commissioning the DRAGON facility at ISAC," *Nuclear Instruments and Methods in Physics Research Section A: Accelerators, Spectrometers, Detectors and Associated Equipment*, vol. 553, pp. 491-500, 11 2005.
- [18] J. M. D'Auria, R. E. Azuma, S. Bishop, L. Buchmann, M. L. Chatterjee, A. A. Chen, S. Engel, D. Gigliotti, U. Greife, D. Hunter, A. Hussein, D. Hutcheon, C. C. Jewett, J. José, J. D. King, A. M. Laird, M. Lamey, R. Lewis, W. Liu, A. Olin, D. Ottewell, P. Parker, J. Rogers, C. Ruiz, M. Trinczek and C. Wrede, "The $^{21}\text{Na}(p,)^{22}\text{Mg}$ reaction from $E_{\text{c.m.}}=200$ to 1103 keV in novae and x-ray bursts," *Physical Review C*, vol. 69, 6 2004.
- [19] W. A. Rolke and A. M. López, "Confidence intervals and upper bounds for small signals in the presence of background noise," *Nuclear Instruments and Methods in Physics Research Section A: Accelerators, Spectrometers, Detectors and Associated Equipment*, vol. 458, pp. 745-758, 2 2001.
- [20] G. J. Feldman and R. D. Cousins, "Unified approach to the classical statistical analysis of small signals," *Physical Review D*, vol. 57, pp. 3873-3889, 4 1998.
- [21] C. Vockenhuber, L. E. Erikson, L. Buchmann, U. Greife, U. Hager, D. A. Hutcheon, M. Lamey, P. Machule, D. Ottewell, C. Ruiz and G. Ruprecht, "A transmission time-of-flight system for particle identification at a recoil mass separator at low energies," *Nuclear Instruments and Methods in Physics Research Section A: Accelerators, Spectrometers, Detectors and Associated Equipment*, vol. 603, pp. 372-378, 5 2009.
- [22] M. Williams, "Measurement of the $^{22}\text{Ne}(p,\gamma)^{23}\text{Na}$ reaction rate using the DRAGON facility and commissioning of the EMMA recoil mass spectrometer", 2019 (University of York). Online: <http://etheses.whiterose.ac.uk/id/eprint/22099>

[23] B. Singh, "Nuclear Data Sheets for $A = 80$," *Nuclear Data Sheets*, vol. 105, pp. 223-418, 6 2005.

[24] T. Rauscher and F.-K. Thielemann, "Astrophysical Reaction Rates From Statistical Model Calculations," *Atomic Data and Nuclear Data Tables*, vol. 75, pp. 1-351, 5 2000.

